Misregulated alternative splicing of *BIN1* is associated with T tubule alterations and muscle weakness in myotonic dystrophy

Charlotte Fugier[1,17], Arnaud F Klein[2,17], Caroline Hammer[1,17], Stéphane Vassilopoulos[2], Ylva Ivarsson[3], Anne Toussaint[1], Valérie Tosch[1], Alban Vignaud[2], Arnaud Ferry[2], Nadia Messaddeq[1], Yosuke Kokunai[4], Rie Tsuburaya[5], Pierre de la Grange[6], Doulaye Dembele[1], Virginie Francois[2], Guillaume Precigout[2], Charlotte Boulade-Ladame[7], Marie-Christine Hummel[1], Adolfo Lopez de Munain[8], Nicolas Sergeant[9], Annie Laquerrière[10], Christelle Thibault[1], François Deryckere[7], Didier Auboeuf[11], Luis Garcia[2], Pascale Zimmermann[3], Bjarne Udd[12–14], Benedikt Schoser[15], Masanori P Takahashi[4], Ichizo Nishino[5], Guillaume Bassez[16], Jocelyn Laporte[1], Denis Furling[2] & Nicolas Charlet-Berguerand[1]

Myotonic dystrophy is the most common muscular dystrophy in adults and the first recognized example of an RNA-mediated disease. Congenital myotonic dystrophy (CDM1) and myotonic dystrophy of type 1 (DM1) or of type 2 (DM2) are caused by the expression of mutant RNAs containing expanded CUG or CCUG repeats, respectively. These mutant RNAs sequester the splicing regulator Muscleblind-like-1 (MBNL1), resulting in specific misregulation of the alternative splicing of other pre-mRNAs. We found that alternative splicing of the bridging integrator-1 (*BIN1*) pre-mRNA is altered in skeletal muscle samples of people with CDM1, DM1 and DM2. BIN1 is involved in tubular invaginations of membranes and is required for the biogenesis of muscle T tubules, which are specialized skeletal muscle membrane structures essential for excitation-contraction coupling. Mutations in the *BIN1* gene cause centronuclear myopathy, which shares some histopathological features with myotonic dystrophy. We found that MBNL1 binds the *BIN1* pre-mRNA and regulates its alternative splicing. *BIN1* missplicing results in expression of an inactive form of BIN1 lacking phosphatidylinositol 5-phosphate–binding and membrane-tubulating activities. Consistent with a defect of BIN1, muscle T tubules are altered in people with myotonic dystrophy, and membrane structures are restored upon expression of the normal splicing form of BIN1 in muscle cells of such individuals. Finally, reproducing *BIN1* splicing alteration in mice is sufficient to promote T tubule alterations and muscle weakness, a predominant feature of myotonic dystrophy.

Myotonic dystrophy is the most common adult-onset muscular dystrophy and comprises two genetically distinct forms: DM1, which is caused by a CTG repeat expansion ranging from ~50 to 1,000 repeats in the 3′ untranslated region of the dystrophia myotonica-protein kinase (*DMPK*) gene[1–3], and DM2, which is caused by expansions of CCTG repeats in the first intron of the *CNBP* (also known as *ZNF9*) gene[4]. Furthermore, CTG expansions over 1,000 repeats are associated with the severe congenital form, CDM1.

Expression of RNAs containing expanded CUG or CCUG repeats interfere with the splicing of other pre-mRNAs through pathological alteration of two classes of RNA binding proteins[5–7]. MBNL1 is sequestered within nuclear RNA aggregates formed by expanded CUG and CCUG repeats[8–10] in individuals with CDM1, DM1 and DM2, whereas expression and phosphorylation of the CUG-binding protein-1 (CUGBP1) have been reported to be increased in individuals with DM1 (ref. 11). MBNL1 and CUGBP1 are RNA splicing factors, and altering their functional levels in myotonic dystrophic tissues results in reversion to embryonic splicing patterns for several mRNAs, such as the muscle chloride channel *CLCN1* and the insulin receptor *INSR*, resulting in myotonia and insulin resistance, respectively[12–14].

However, the cause of the progressive muscle weakness, which is a cardinal symptom of myotonic dystrophy, remains ill defined. Notably, the histopathological features of individuals with CDM1 (muscle fiber atrophy with centrally located nuclei in absence of regeneration) are similar to those of centronuclear myopathy (CNM)[15]. CNM's are caused by mutations in the myotubularin (*MTM1*), dynamin-2 (*DNM2*) and *BIN1* genes[16–18]. BIN1, also known as amphiphysin 2,

[1]Institut de Génétique et de Biologie Moléculaire et Cellulaire (IGBMC), Institut National de la Santé et de la Recherche Médicale (INSERM) U964, Centre National de la Recherche Scientifique (CNRS) UMR7104, University of Strasbourg, Illkirch, France. [2]Université Pierre et Marie Curie, University Paris 06, UM76, Institut de Myologie, INSERM U974 and CNRS UMR7215, Paris, France. [3]Department of Human Genetics, KU Leuven, Leuven, Belgium. [4]Department of Neurology, Osaka University Graduate School of Medicine, Osaka, Japan. [5]National Center of Neurology and Psychiatry, Tokyo, Japan. [6]GenoSplice technology, Hôpital Saint-Louis, Paris, France. [7]CNRS UMR7175, Université Louis Pasteur, Oncoprotéines, Ecole Supérieure de Biotechnologies de Strasbourg, Illkirch, France. [8]Hospital Donostia, Biodonostia Institute, Centro de Investigación Biomédica en Red sobre Enfermedades Neurodegenerativas–Instituto Carlos III, San Sebastián, Spain. [9]INSERM U837-1, Jean Pierre Aubert Research Center, Alzheimer and Tauopathies, Lille, France. [10]Pathology Laboratory, University Hospital of Rouen, Rouen, France. [11]INSERM U590, Centre Léon Bérard, Lyon, France. [12]Neuromuscular Research Center, Tampere University, Tampere, Finland. [13]Folkhälsan Institute of Genetics, Department of Medical Genetics, Helsinki University, Helsinki, Finland. [14]Department of Neurology, Vasa Central Hospital, Vasa, Finland. [15]Friedrich Baur Institute, Ludwig Maximilian University, Munich, Germany. [16]INSERM U955, Institut Mondor de Recherche Biomédicale, Créteil, France. [17]These authors contributed equally to this work. Correspondence should be addressed to N.C.-B. (ncharlet@igbmc.fr).

Received 28 December 2010; accepted 6 April 2011; published online 29 May 2011; doi:10.1038/nm.2374

is a protein specialized in membrane curvature whose function is regulated by alternative splicing (**Fig. 1a** and **Supplementary Fig. 1**). In skeletal muscles, inclusion of the muscle-specific exon 11, which encodes a phosphoinositide-binding domain[19], generates an isoform of BIN1 that induces tubular invaginations of membranes[19,20] and is implicated in T tubule biogenesis[19–21]. The T tubule network is a specialized membrane structure fundamental for excitation-contraction coupling in skeletal muscle, and disruption of *BIN1* in *Drosophila melanogaster* leads to disorganization of these structures and the dysfunction of the associated excitation-contraction coupling machinery[21].

Using whole-genome microarrays, we identified a robust misregulation of alternative splicing of the *BIN1* pre-mRNA in primary cultures of differentiated CDM1 muscle cells (**Supplementary Fig. 1a**). RT-PCR confirmed that exon 11 of *BIN1* mRNA was mostly skipped in skeletal muscles of individuals with myotonic dystrophy and that *BIN1* misregulation correlated with disease severity, as *BIN1* exon 11 was absent in severe congenital CDM1 but partially skipped in the milder adult DM1 and DM2 forms (**Fig. 1b,c**). As described for other misregulated splicing events identified in individuals with myotonic dystrophy, the skipping of *BIN1* exon 11 was also observed in embryonic skeletal muscles of control individuals (**Supplementary Fig. 1d,e**), suggesting that myotonic dystrophy may result from the failure to complete the developmental switch of a specific set of alternative splicing events.

Note that the misregulation of *BIN1* alternative splicing was specific to myotonic dystrophy, as we did not find it in muscle samples from people with amyotrophic lateral sclerosis (**Fig. 1c**). And it did not result from a global alteration of the splicing machinery, as we found no splicing alterations of *MTM1*, *DNM2* and *BIN1* brain-specific exons 13 to 16 in muscle samples from individuals with DM1 (data not shown). Finally, western blot analysis showed a reduction in the BIN1 protein isoform containing exon 11 in individuals with CDM1 and confirmed that this splicing misregulation did not alter the global level of BIN1 protein expression (**Fig. 1d**).

To determine the mechanisms underlying alterations of *BIN1* splicing, we constructed a minigene containing the exon 11 of *BIN1* bordered by its intronic regions and concurrently expressed it with a separate vector expressing only expanded CUG or CCUG repeats. Overexpression of ~1,000 CUG or 300 CCUG repeats repressed exon 11 inclusion, whereas the expression of a control plasmid containing the 3′ untranslated region of *DMPK* with no CTG repeats had no effect (**Fig. 2a**), indicating that expression of CUG or CCUG repeats was sufficient to induce *BIN1* splicing alteration. Depletion of MBNL1 by an siRNA-mediated approach mimicked the effect of CUG or CCUG repeats and promoted exon 11 exclusion, whereas overexpression of MBNL1 stimulated exon 11 inclusion (**Fig. 2a**). In contrast, overexpression or depletion of CUGBP1 had little effect on exon 11 inclusion (**Fig. 2a**). Similar dichotomous results between the effects of overexpression of MBNL1 and CUGBP1 have been reported with *INSR*, *CLCN1*, troponin T type 3 (skeletal, fast) (*Tnnt3*) and ATPase, Ca^{2+} transporting, cardiac muscle, fast twitch-1 (*ATP2A1*) minigenes[22–25], and only a subset of splicing events are co-regulated by CUGBP1 and MBNL1 (ref. 26), suggesting that the sole sequestration of MBNL1 is sufficient to induce splicing misregulation in myotonic dystrophy[27]. Consistent with the crystal structure of MBNL1 zinc fingers[28], MBNL1 recognized single-stranded UGC RNA motifs located downstream of *BIN1* exon 11 (**Fig. 2b** and **Supplementary Fig. 2b**). Mutation of MBNL1 binding sites reduced the responsiveness of the *BIN1* minigene to MBNL1, but also to expanded CUG or CCUG repeats (**Fig. 2c**), indicating that the *trans*-dominant effect of expanded CUG and CCUG repeats on splicing misregulation requires functional MBNL1 binding sites. Finally, binding of MBNL1 to the UGC motifs present in intron 11 of *BIN1* was competed by an excess of unlabeled expanded CUG repeats (**Fig. 2d**), which is consistent with the model of myotonic dystrophy in which an excess of expanded CUG or CCUG repeats reduces the quantity of free MBNL1 and, consequently, the binding of MBNL1 to its physiological RNA targets.

BIN1 protein is involved in membrane binding and curvature[19–21], and its muscle-specific exon 11 encodes a phosphoinositide-binding domain[19]. To investigate the consequences of *BIN1* exon 11 skipping for myotonic dystrophy, we first examined the tubulating activity of BIN1. As previously observed[18–21], overexpression of a plasmid containing the EGFP-tagged normal muscle splicing form of BIN1 (with exon 11) in C2C12 differentiated muscle cells induced the formation of

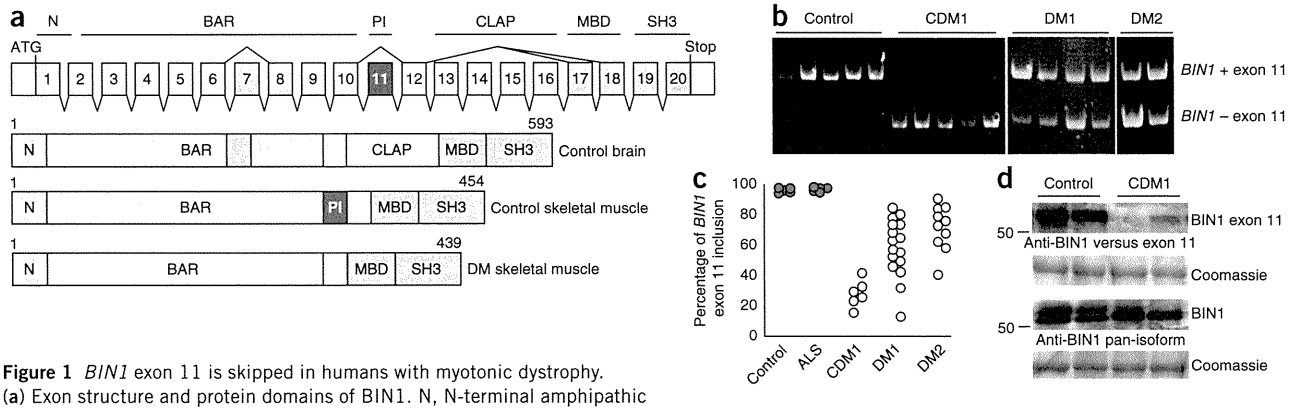

Figure 1 *BIN1* exon 11 is skipped in humans with myotonic dystrophy. (**a**) Exon structure and protein domains of BIN1. N, N-terminal amphipathic helix; BAR, BIN1-amphiphysin-Rvs167; PI, phosphoinositide-binding domain; CLAP, clathrin-associated protein–binding domain; MBD, Myc-binding domain; SH3, Src homology 3. The skeletal muscle–specific splicing form of BIN1 lacks the brain-specific CLAP domain but includes the muscle-specific PI-binding domain encoded by exon 11. (**b**) Representative RT-PCR analysis of endogenous *BIN1* mRNA from human skeletal muscle biopsies of normal adult individuals (control), fetuses with CDM1, and adults with DM1 and DM2. (**c**) Graphical representation of the RT-PCR analysis depicting the percentage of *BIN1* mRNA including exon 11 in skeletal muscle samples from normal individuals and individuals with amyotrophic lateral sclerosis (ALS), CDM1 (fetuses from 20 weeks to birth), DM1 (infants and adults) and DM2 (adults). (**d**) Representative western-blotting analysis of endogenous BIN1 protein from skeletal muscle samples of normal and age-matched fetuses with CDM1. Top, BIN1 was detected with an antibody directed against exon 11 (Anti-BIN1 versus exon 11). Middle, BIN1 was detected with the pan-isoform antibody directed against exon 17 (Anti-Bin1 pan-isoform). Equal loading was monitored by Coomassie staining. Similar results were obtained in four independent experiments.

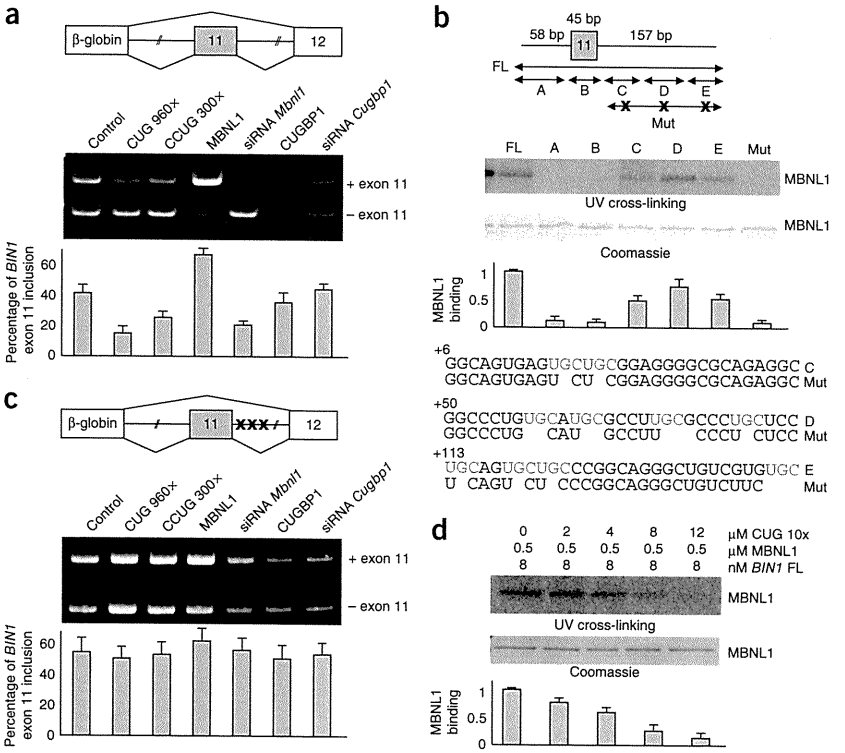

Figure 2 MBNL1 stimulates inclusion of *BIN1* exon 11. (**a**) Top, a schematic showing a *BIN1* minigene containing exon 11 bordered by 235 nucleotides of its upstream intron 10 and 226 nucleotides of its downstream intron 11. Middle, RT-PCR analysis of this minigene coexpressed with a plasmid expressing a *DMPK* minigene lacking CUG repeats (control), expressing 960 CUG repeats, 300 CCUG, GFP-MBNL1 or GFP-CUGBP1 or with siRNA directed against *Mbnl1* or against *Cugbp1* in C2C12 cells differentiated 24 h. Bottom, the mean of at least three independent transfections is depicted as the percentage of mRNA containing *BIN1* exon 11. Error bars indicate s.d. (**b**) Top, the RNAs derived from the *BIN1* minigene include nonoverlapping segments (A–E) of 58, 45, 43, 51 and 63 nucleotides, respectively. Middle, UV cross-linking assays done with 0.5 μg of purified bacterial recombinant GST-MBNL1Δ and RNAs uniformly labeled with ^{32}P-CTP. PhosphorImager exposition, Coomassie staining and quantification of at least three independent UV cross-linking assays are depicted as the intensity of MBNL1 binding relative to *BIN1* full-length (FL) RNA. Bottom, sequences of the wild-type and mutant RNAs used in the UV cross-linking experiments. (**c**) A *BIN1* minigene containing mutations of the UCG motifs in the downstream intron, analyzed as in **a**. (**d**) UV cross-linking binding of 0.5 μg of purified bacterial recombinant GST-MBNL1Δ to full-length *BIN1* RNA uniformly labeled with ^{32}P-CTP and competed by increasing amounts of unlabeled RNA containing ten CUG repeats. PhosphorImager exposition, Coomassie staining and quantification of three independent UV cross-linking assays are depicted as the intensity of MBNL1 binding relative to *BIN1* full-length RNA. Error bars in **a**–**d** indicate s.d.

numerous narrow tubular membrane structures (**Fig. 3a**). In contrast, expression of the splicing isoform of BIN1 (without exon 11) found in individuals with myotonic dystrophy produced little to no tubules, resulting in a diffuse cytoplasmic localization of BIN1 (**Fig. 3a**). We obtained identical results in nonmuscle cells (**Supplementary Fig. 3a**). Next, we tested the phosphoinositide-binding activity of the splicing forms of BIN1 containing or excluding exon 11. Lipid dot-blot assays (**Supplementary Fig. 3b**) and surface plasmon resonance experiments (**Fig. 3b**) showed that GST-tagged purified recombinant protein of the normal muscle isoform of BIN1 (with exon 11) recognized with high affinity phosphatidylinositol-5-phosphate (PtdIns5P) and phosphatidylinositol-3-phosphate (PtdIns3P) compared to phosphatidylinositol-4,5-biphosphate (PtdIns(4,5)P2) (apparent K_d values of 620 ± 20 nM, 660 ± 60 nM and 1,100 ± 100 nM, respectively). In contrast, the isoform of BIN1 found in individuals with myotonic dystrophy (without exon 11) had lost most of its ability to bind phosphoinositides (**Fig. 3b** and **Supplementary Fig. 3b**).

The similar affinity of BIN1 with exon 11 for PtdIns5P and PtdIns3P *in vitro* raises the question of whether BIN1 recognizes both phosphoinositides in cell culture. Transduction of muscle cell primary cultures with adenovirus expressing an EGFP-tagged probe for PtdIns5P, PtdIns3P or PtdIns(4,5)P2 revealed that the normal BIN1 isoform (with exon 11) colocalized with tubule structures containing PtdIns5P but not with endosomal vesicles containing PtdIns3P or with the plasma membrane enriched in PtdIns(4,5)P2 (**Supplementary Fig. 3c**), suggesting that BIN1 recognizes mostly PtdIns5P in muscle cells. Because mutations in the *MTM1* gene, which codes for the phosphatase responsible of PtdIns5P production[29], cause CNM[16], we propose that this phosphoinositide is enriched in BIN1-membrane structures and may constitute a functional link between BIN1 and MTM1.

The alteration of the activities of BIN1 *in vitro* and in cell culture made us wonder whether BIN1 functions are also altered in humans with myotonic dystrophy. In skeletal muscle, BIN1 is involved in the organization of the T tubule network[19–21], a specialized membrane structure fundamental for excitation-contraction coupling. As noted previously[19,21], immunofluorescence analysis of control human muscles showed that BIN1 was organized in transversal projections, which localized with the L-type calcium channel CACNA1S (also known as DHPRα1 or CAV1.1), a major component of T tubules (**Fig. 3c** and **Supplementary Fig. 3d**). In contrast, BIN1 was disorganized and presented a more diffuse localization in age-matched DM1 muscles (**Fig. 3c** and **Supplementary Fig. 3e**). CACNA1S localization was also slightly altered in DM1 muscle fibers (**Fig. 3c**), whereas labeling of ACTN1 (α-actinin-1), which is a marker of muscle fiber Z lines, was not altered (**Supplementary Fig. 3e**). As previously reported[30], ultrastructural analysis confirmed alterations of the T tubule network in DM1 muscles, with the presence of irregular and longitudinally orientated T tubules (**Fig. 3d**). Consistent with an alteration of BIN1 function, we observed a diffuse cytoplasmic localization of BIN1 and no or few BIN1 tubules in differentiated muscle cells isolated from humans with CDM1 and DM1 compared to control myotubes (**Fig. 3e**).

To test whether the absence of BIN1 structures observed in myotonic dystrophic muscle cells can be restored, we transduced CDM1 myotubes with an adenovirus expressing either the isoform of BIN1 found in normal individuals (with exon 11) or in individuals with myotonic dystrophy (without exon 11). Control BIN1 induced numerous BIN1 tubules in CDM1 myotubes, whereas expression of the splicing

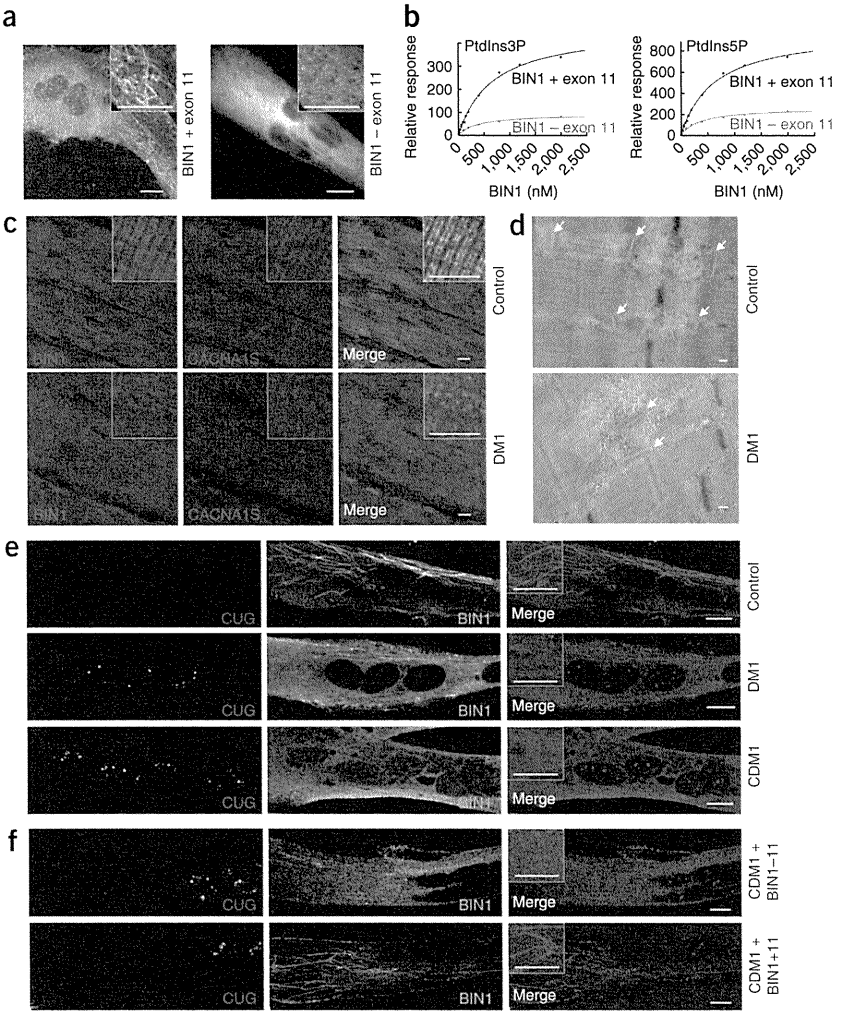

Figure 3 The splicing form of BIN1 expressed in myotonic dystrophic patients is inactive. (**a**) Representative images from confocal projections of differentiated C2C12 cells transfected with a plasmid expressing EGFP-BIN1 including or excluding exon 11. Insets, higher magnifications of GFP-BIN1 localization. Scale bars, 10 μm. (**b**) Surface plasmon resonance equilibrium titrations of full-length GST-BIN1 including or excluding exon 11 binding to 5% PtdIns5P and PtdIns3P in dioleoylphosphatidylcholine (DOPC) liposomes. The data were fitted by nonlinear regression analysis to the Langmuir binding isotherm. (**c**) Representative confocal images of immunofluorescence labeling of BIN1 and CACNA1S in paraffin-embedded longitudinal sections of skeletal muscles from an adult with DM1 and an age-matched control individual. Insets, higher magnifications of BIN1 and CACNA1S localizations. Scale bars, 10 μm. (**d**) Representative electron microscopy images of longitudinal sections of skeletal muscle from an adult with DM1 and an age-matched control individual. White arrows indicate T tubule structures. Scale bars, 100 nm. (**e**) Representative confocal images of RNA fluorescence *in situ* hybridization (FISH) using a Cy3-(CAG)7x PNA probe to detect CUG aggregates coupled to immunofluorescence detection of BIN1 of 6-d differentiated human skeletal muscle cells originating from a control individual, a person with DM1 (1,300 CTG repeats) and a person with CDM1 (2,000 CTG repeats). Nuclei are labeled by DAPI (blue) staining. Insets, higher magnifications of BIN1 localization. Scale bars, 10 μm. (**f**) Representative confocal images of RNA FISH labeling of CUG expanded repeats in CDM1 differentiated skeletal muscle cells transduced (multiplicity of infection of 1,500) with recombinant adenovirus expressing cDNA constructs of GFP-BIN1 containing or excluding exon 11. Insets, higher magnifications of GFP-BIN1 localization. Scale bars, 10 μm.

variant of BIN1 found in people with myotonic dystrophy did not (**Fig. 3f** and **Supplementary Fig. 3f**). Overall, these results indicate that the myotonic dystrophic splicing form of BIN1, which lacks exon 11, has lost most of its membrane binding and tubulating properties, and they suggest that T tubules are misorganized in myotonic dystrophic skeletal muscles and that expression of the normal splice form of BIN1 is sufficient to induce normal membrane structures.

Various altered splicing events have been reported in myotonic dystrophy, making unclear the importance of BIN1 misregulation. To test the consequences of the splicing alteration of *BIN1*, we artificially forced the skipping of *Bin1* exon 11 in mouse skeletal muscle through an exon-skipping strategy[31]. We cloned a modified U7 small nuclear RNA construct harboring an antisense sequence (U7-ex11AS), which specifically promoted skipping of *Bin1* exon 11 (**Fig. 4a** and **Supplementary Fig. 4a**), into an adeno-associated virus backbone (AAV2/1). We injected tibialis anterior muscles of wild-type newborn mice with U7-ex11AS virus, whereas we injected contralateral muscles with vehicle alone or with control AAV2/1. We analyzed the muscles 4 months after injection. Expression of U7-ex11AS reproduced the splicing alteration of *BIN1* observed in humans with myotonic dystrophy but did not induce other splicing changes (**Fig. 4b**), suggesting that this AAV2/1 exon 11 skipping strategy did not induce a global embryonal re-adaptation or any severe muscle degeneration or regeneration changes. Immunofluorescence analysis revealed that artificial skipping of *Bin1* exon 11 promoted Bin1 mislocalization and slight alterations of Cacna1s organization (**Fig. 4c**) compared to control-injected contralateral muscles. Markers of muscle Z lines, such as α-actinin and desmin, were not altered in U7-ex11AS–injected or control AAV2/1–injected muscles (data not shown), indicating that muscle integrity was maintained. Further histopathological and ultrastructural analyses revealed no major atrophy or degeneration of muscle fibers and normal mitochondrion and sarcomere structures (**Fig. 4d** and **Supplementary Fig. 4b**). In contrast, osmium tetroxide–potassium ferricyanide staining showed that ~30% of T tubules were abnormal in *Bin1* exon 11–skipped muscles, with longitudinally oriented, disorganized and irregular structures (**Fig. 4d** and **Supplementary Fig. 4c**).

These results suggest that alteration of the T tubule network is an early and specific event following *Bin1* exon 11 alteration. Notably, isometric strength measurement of the tibialis anterior muscles showed that skipping of *Bin1* exon 11 induced a ~28% decrease ($n = 11$, $P = 0.00034$) in specific muscle strength (**Fig. 4e**). We noted some variability in *Bin1* exon 11 skipping inherent to the AAV exon-skipping strategy[31], which is a milder approach compared to lethal

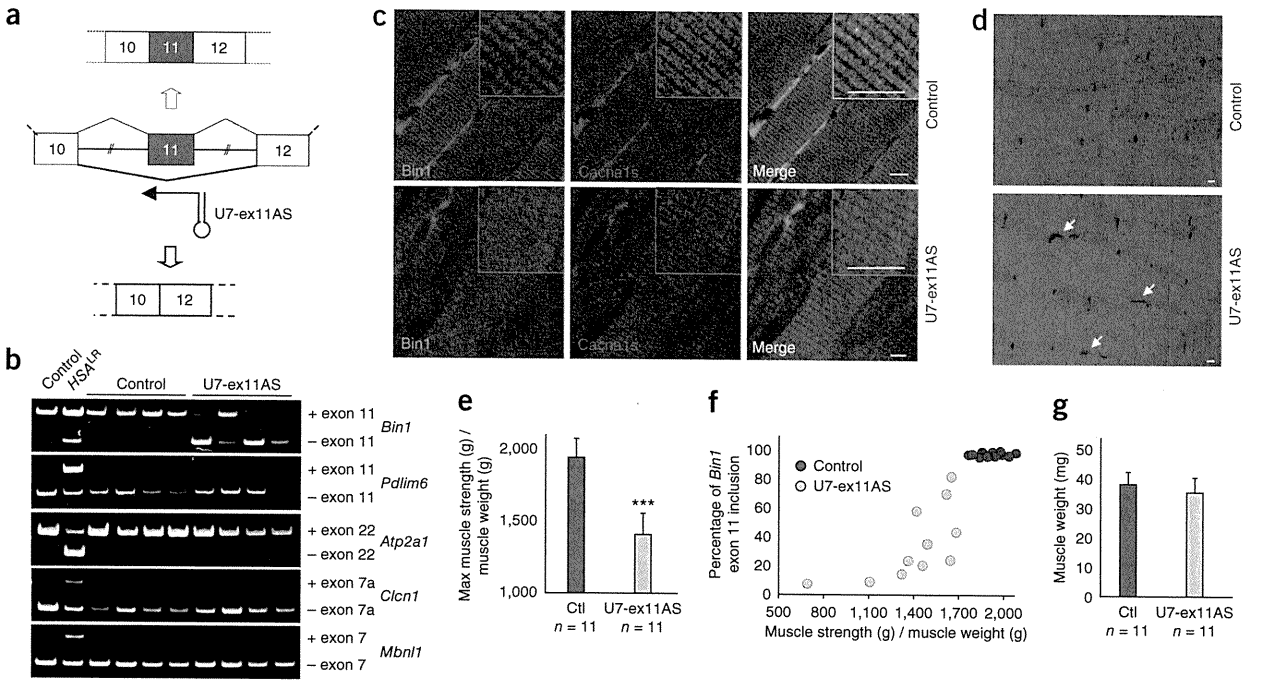

Figure 4 Skipping of *Bin1* exon 11 is sufficient to induce muscle weakness in mice. (**a**) Schematic representation of the U7-exon 11 antisense construct (U7-ex11AS). (**b**) RT-PCR analysis of *Bin1* exon 11, *Pdlim6* (encoding Ldb3, also known as Zasp or cypher) exon 11, *Atp2a1* exon 22, *Clcn1* exon 7a and *Mbnl1* exon 7 from total RNA extracted from tibialis anterior muscles of wild-type mice 4 months after injection of control AAV2/1 or AAV2/1 encoding the U7-ex11AS construct. RNA samples of transgenic mice expressing 250 expanded CUG repeats in skeletal muscle (HSA^{LR} mice)[6] were used as a positive control. (**c**) Confocal microscopy analysis of immunofluorescence labeling of Bin1 and Cacna1s in longitudinal paraffin-embedded sections of TA muscle injected with control AAV2/1 or AAV2/1 encoding the U7-ex11AS construct. Insets, higher magnifications of Bin1 localization. Scale bars, 10 μm. (**d**) Electron microscopy analysis of osmium tetroxide–potassium ferricyanide–stained longitudinal sections of tibialis anterior muscles of wild-type mice 4 months after injection of control AAV2/1 or AAV2/1 encoding the U7-ex11AS construct. White arrows indicate altered T tubule structures. Scale bars, 100 nm. (**e–g**) Measures of the absolute maximal isometric tetanic force (**e**), of the tetanic force relative to the inclusion of *Bin1* exon 11 (**f**) and of the muscle weight (**g**) of isolated TA muscle injected with vehicle alone (PBS, $n = 2$), AAV2/1 expressing a control construct ($n = 9$) or AAV2/1 expressing the U7-ex11AS construct ($n = 11$). As no differences between vehicle alone ($n = 2$) or control AAV2/1 ($n = 9$) were observed, data were pooled and are indicated as generic control ($n = 11$). Data are presented as means ± s.d. $^{***}P < 0.001$.

knockout of *Bin1* (ref. 32). The extent of muscle weakness correlated ($R^2 = 0.62$) with the degree of *Bin1* exon 11 skipping (**Fig. 4f**), suggesting a direct correlation between *Bin1* splicing misregulation and muscle weakness. This is reminiscent of our findings in people with myotonic dystrophy, in whom we observed near-complete BIN1 exon 11 absence in the severe congenital CDM1 form, whereas we saw only partial splicing alteration in the milder adult DM1 and DM2 forms. Although muscle weakness was evident in the mice with exon 11 skipping, we observed no significant muscle mass loss 4 months after injection (**Fig. 4g**), suggesting that T tubule alterations and muscle weakness preceded muscle atrophy or degeneration. In addition, we observed similar Bin1 mislocalization and muscle weakness when we injected muscles of adult wild-type mice (**Supplementary Fig. 4d–f**), suggesting that Bin1 is required both postnatally and in adulthood.

T tubule alterations and muscle weakness have also been reported in a CNM mouse model in which the *Mtm1* gene was deleted[33]. These alterations were accompanied by a decreased expression of Cacna1s, spurring us to determine whether similar changes occurred in our *Bin1* model. Quantitative RT-PCR and western blotting showed a significant ($P < 0.05$) decrease in Cacna1s expression in muscles injected with U7-ex11AS virus compared to control contralateral-injected muscles (**Supplementary Fig. 4g,h**). Overall, these results suggest that misregulation of *Bin1* exon 11 splicing is sufficient to induce alterations of T tubules and of Cacna1s, a key regulator of the excitation-contraction coupling process, ultimately resulting in muscle weakness.

In conclusion, our results suggest a model (**Supplementary Fig. 5**) in which the alternative splicing of the muscle-specific exon 11 of *BIN1* mRNA is regulated by the MBNL1 splicing factor. Sequestration of MBNL1 by expanded CUG or CCUG repeats in individuals with DM1 or DM2, respectively, leads to skipping of that exon and expression of an isoform of BIN1 unable to bind PtdIns5P and tubulate membranes, which ultimately results in disorganized T tubules and altered excitation-contraction coupling. We propose that missplicing of *BIN1* and of other pre-mRNAs involved in excitation-contraction coupling[34] (ryanodine receptor 1 (skeletal) (*RYR1*), *ATP2A1*, *ATP2A2* and so on) ultimately results in muscle weakness in humans with myotonic dystrophy. This model is consistent with previous finding of T tubule alterations[30] and calcium homeostasis alterations[34,35] in muscle cells in humans with, and mouse models of, myotonic dystrophy. Furthermore, we propose that the MTM1 phosphatase produces PtdIns5P-enriched membranes, which are recognized by exon 11 of BIN1, resulting in membrane tubulation (**Supplementary Fig. 5**). This model is consistent with previous reports of T tubule elongation through accretion of cytoplamic vesicles[36], recent observations of BIN1 and T tubule alterations in humans with, and animal models of, CNM[33,37,38] and case reports of congenital myopathies with central nuclei resulting from mutations in *RYR1* (ref. 39). These data suggest that a common

mechanism, involving T tubule biogenesis by BIN1 leading to alterations of the calcium homeostasis coupled to the excitation-contraction process, may underlie muscle weakness in myotonic dystrophy and centronuclear myopathy.

METHODS

Methods and any associated references are available in the online version of the paper at http://www.nature.com/naturemedicine/.

Accession codes. Microarray data have been deposited in the Gene Expression Omnibus (GEO) with accession code GSE21795.

Note: Supplementary information is available on the Nature Medicine website.

ACKNOWLEDGMENTS

We thank T. Cooper (Baylor College of Medicine) for the gift of the β-globin 4.11.12, DMPKS, DT960 and tgCUGBP1 plasmids, L. Ranum (University of Minnesota) for the gift of the CCTG300 expression plasmid, C. Branlant (CNRS) for the gift of the pGEX-MBNL1Δ101 vector, M. Swanson (University of Florida) for the gift of the pGEX-6P-MBNL1-His vector, P. Hawkins (Babraham Research Campus) for the gift of the GFP-PH domain of PLCg and GFP-PX domain of P40 constructs, O. Gozani (Stanford University) for the gift of the GFP-PHD domain of ING2 vector, Z. Xue (Université Paris 7) for the gift of the synemin-specific antibody, I. Marty (INSERM) for the gift of the RYR1-specific antibody, M. Swanson (University of Florida), G. Gourdon (INSERM) and C. Thornton (University of Rochester) for the gift of RNA from skeletal muscles of MBNL1$^{\Delta E3}$, DM300 and HSA^{LR} mice, respectively, the IGBMC facilities for assistance, J. Lainé, G. Butler-Browne and all members of the French DM Network for fruitful discussion. This work was supported by INSERM AVENIR (N.C.-B.), Agence nationale de la recherche GENOPAT 07-942 (N.C.-B.), 08-005 (J.L.) and BLANC 07-065 (J.L.), Association Française contre les Myopathies MNM1 12982 (N.C.-B.), 12570 and 14269 (D.F.), 12576 and 14058 (J.L.), Fondation pour la Recherche Médicale 20071210538 (J.L.), Japan Society for the Promotion of Science KAKENHI 20590998 (M.P.T.) and a European Molecular Biology Organization long-term fellowship (Y.I.).

AUTHOR CONTRIBUTIONS

Experiments were carried out by C.F., A.F.K., C.H., S.V., Y.I., A.T., V.T., A.V., A.F., N.M., Y.K., R.T., V.F., G.P., C.B.-L. F.D. and M.-C.H. Bioinformatic analyses were done by P.d.l.G., D.D., C.T. and D.A. Clinical samples and patient data were from A.L.d.M., N.S., A.L., B.U., B.S., M.P.T., I.N., G.B. and D.F. Data were collected and analyzed by N.M., C.T., D.A., L.G., P.Z., I.N., M.P.T., B.U., B.S., G.B., J.L., D.F. and N.C.-B. The study was designed, coordinated and written by D.F. and N.C.-B.

COMPETING FINANCIAL INTERESTS

The authors declare no competing financial interests.

Published online at http://www.nature.com/naturemedicine/.
Reprints and permissions information is available online at http://www.nature.com/reprints/index.html.

1. Brook, J.D. *et al.* Molecular basis of myotonic dystrophy: expansion of a trinucleotide (CTG) repeat at the 3′ end of a transcript encoding a protein kinase family member. *Cell* **68**, 799–808 (1992).
2. Fu, Y.H. *et al.* An unstable triplet repeat in a gene related to myotonic muscular dystrophy. *Science* **255**, 1256–1258 (1992).
3. Mahadevan, M. *et al.* Myotonic dystrophy mutation: an unstable CTG repeat in the 3′ untranslated region of the gene. *Science* **255**, 1253–1255 (1992).
4. Liquori, C.L. *et al.* Myotonic dystrophy type 2 caused by a CCTG expansion in intron 1 of ZNF9. *Science* **293**, 864–867 (2001).
5. Philips, A.V., Timchenko, L.T. & Cooper, T.A. Disruption of splicing regulated by a CUG-binding protein in myotonic dystrophy. *Science* **280**, 737–741 (1998).
6. Mankodi, A. *et al.* Myotonic dystrophy in transgenic mice expressing an expanded CUG repeat. *Science* **289**, 1769–1773 (2000).
7. Seznec, H. *et al.* Mice transgenic for the human myotonic dystrophy region with expanded CTG repeats display muscular and brain abnormalities. *Hum. Mol. Genet.* **10**, 2717–2726 (2001).
8. Miller, J.W. *et al.* Recruitment of human muscleblind proteins to (CUG)*n* expansions associated with myotonic dystrophy. *EMBO J.* **19**, 4439–4448 (2000).
9. Kanadia, R.N. *et al.* A muscleblind knockout model for myotonic dystrophy. *Science* **302**, 1978–1980 (2003).
10. Ho, T.H. *et al.* Muscleblind proteins regulate alternative splicing. *EMBO J.* **23**, 3103–3112 (2004).
11. Kuyumcu-Martinez, N.M., Wang, G.S. & Cooper, T.A. Increased steady-state levels of CUGBP1 in myotonic dystrophy 1 are due to PKC-mediated hyperphosphorylation. *Mol. Cell* **28**, 68–78 (2007).
12. Savkur, R.S., Philips, A.V. & Cooper, T.A. Aberrant regulation of insulin receptor alternative splicing is associated with insulin resistance in myotonic dystrophy. *Nat. Genet.* **29**, 40–47 (2001).
13. Mankodi, A. *et al.* Expanded CUG repeats trigger aberrant splicing of ClC-1 chloride channel pre-mRNA and hyperexcitability of skeletal muscle in myotonic dystrophy. *Mol. Cell* **10**, 35–44 (2002).
14. Charlet-Berguerand, N. *et al.* Loss of the muscle-specific chloride channel in type 1 myotonic dystrophy due to misregulated alternative splicing. *Mol. Cell* **10**, 45–53 (2002).
15. Jungbluth, H., Wallgren-Pettersson, C. & Laporte, J. Centronuclear (myotubular) myopathy. *Orphanet J. Rare Dis.* **3**, 26 (2008).
16. Laporte, J. *et al.* A gene mutated in X-linked myotubular myopathy defines a new putative tyrosine phosphatase family conserved in yeast. *Nat. Genet.* **13**, 175–182 (1996).
17. Bitoun, M. *et al.* Mutations in dynamin 2 cause dominant centronuclear myopathy. *Nat. Genet.* **37**, 1207–1209 (2005).
18. Nicot, A.S. *et al.* Mutations in amphiphysin 2 (BIN1) disrupt interaction with dynamin 2 and cause autosomal recessive centronuclear myopathy. *Nat. Genet.* **39**, 1134–1139 (2007).
19. Lee, E. *et al.* Amphiphysin 2 (BIN1) and T tubule biogenesis in muscle. *Science* **297**, 1193–1196 (2002).
20. Peter, B.J. *et al.* BAR domains as sensors of membrane curvature: the amphiphysin BAR structure. *Science* **303**, 495–499 (2004).
21. Razzaq, A. *et al.* Amphiphysin is necessary for organization of the excitation-contraction coupling machinery of muscles, but not for synaptic vesicle endocytosis in *Drosophila*. *Genes Dev.* **15**, 2967–2979 (2001).
22. Dansithong, W. *et al.* MBNL1 is the primary determinant of focus formation and aberrant insulin receptor splicing in DM1. *J. Biol. Chem.* **280**, 5773–5780 (2005).
23. Hino, S. *et al.* Molecular mechanisms responsible for aberrant splicing of SERCA1 in myotonic dystrophy type 1. *Hum. Mol. Genet.* **16**, 2834–2843 (2007).
24. Yuan, Y. *et al.* Muscleblind-like 1 interacts with RNA hairpins in splicing target and pathogenic RNAs. *Nucleic Acids Res.* **35**, 5474–5486 (2007).
25. Kino, Y. *et al.* MBNL and CELF proteins regulate alternative splicing of the skeletal muscle chloride channel CLCN1. *Nucleic Acids Res.* **37**, 6477–6490 (2009).
26. Kalsotra, A. *et al.* A postnatal switch of CELF and MBNL proteins reprograms alternative splicing in the developing heart. *Proc. Natl. Acad. Sci. USA* **105**, 20333–20338 (2008).
27. Kanadia, R.N. *et al.* Reversal of RNA missplicing and myotonia after muscleblind overexpression in a mouse poly(CUG) model for myotonic dystrophy. *Proc. Natl. Acad. Sci. USA* **103**, 11748–11753 (2006).
28. Teplova, M. & Patel, D.J. Structural insights into RNA recognition by the alternative-splicing regulator muscleblind-like MBNL1. *Nat. Struct. Mol. Biol.* **15**, 1343–1351 (2008).
29. Tronchère, H. *et al.* Production of phosphatidylinositol 5-phosphate by the phosphoinositide 3-phosphatase myotubularin in mammalian cells. *J. Biol. Chem.* **279**, 7304–7312 (2004).
30. Ueda, H. *et al.* Decreased expression of myotonic dystrophy protein kinase and disorganization of sarcoplasmic reticulum in skeletal muscle of myotonic dystrophy. *J. Neurol. Sci.* **162**, 38–50 (1999).
31. Goyenvalle, A. *et al.* Rescue of dystrophic muscle through U7 snRNA-mediated exon skipping. *Science* **306**, 1796–1799 (2004).
32. Muller, A.J. *et al.* Targeted disruption of the murine Bin1/amphiphysin II gene does not disable endocytosis but results in embryonic cardiomyopathy with aberrant myofibril formation. *Mol. Cell. Biol.* **23**, 4295–4306 (2003).
33. Al-Qusairi, L. *et al.* T tubule disorganization and defective excitation-contraction coupling in muscle fibers lacking myotubularin lipid phosphatase. *Proc. Natl. Acad. Sci. USA* **106**, 18763–18768 (2009).
34. Kimura, T. *et al.* Altered mRNA splicing of the skeletal muscle ryanodine receptor and sarcoplasmic/endoplasmic reticulum Ca^{2+}-ATPase in myotonic dystrophy type 1. *Hum. Mol. Genet.* **14**, 2189–2200 (2005).
35. Osborne, R.J. *et al.* Transcriptional and post-transcriptional impact of toxic RNA in myotonic dystrophy. *Hum. Mol. Genet.* **18**, 1471–1481 (2009).
36. Yuan, S. *et al.* Biogenesis of transverse tubules: immunocytochemical localization of a transverse tubular protein (TS28) and a sarcolemmal protein (SL50) in rabbit skeletal muscle developing in situ. *J. Cell Biol.* **110**, 1187–1198 (1990).
37. Dowling, J.J. *et al.* Loss of myotubularin function results in T tubule disorganization in zebrafish and human myotubular myopathy. *PLoS Genet.* **5**, e1000372 (2009).
38. Toussaint, A. *et al.* Defects in amphiphysin 2 (BIN1) and triads in several forms of centronuclear myopathies. *Acta Neuropathol.* **121**, 253–266 (2010).
39. Wilmshurst, J.M. *et al.* RYR1 mutations are a common cause of congenital myopathies with central nuclei. *Ann. Neurol.* **68**, 717–726 (2010).

ONLINE METHODS

RT-PCR analysis of *BIN1*. In accordance with the Helsinki Declaration, all human samples were collected after informed consent and with the appropriate oversight of the ethical committees of the following institutions: the Department of Neurology of the University of Osaka, the Center of Neurology and Psychiatry of Tokyo, the Centro de Investigación Biomédica en Red Sobre Enfermedades Neurodegenerativas, the Jean Pierre Aubert Research Center, the Department of Pathology of the University of Rouen, the Department of Neuromuscular Research of the University of Tampere, the Friedrich Baur Institute of the University Ludwig Maximilian and the Institut Mondor de Recherche Biomédicale. Total RNA isolated from homogenized skeletal muscle was subjected to RT–PCR analysis using primers that anneal within human *BIN1* exon 10 (forward: 5′-AGAACCTCAATGATGTGCTGG-3′) and *BIN1* exon 12 (reverse: 5′-TCGTGGTTGACTCTGATCTCGG-3′), resulting in PCR products of 208 bp (+ exon 11) and 163 bp (– exon 11). For mouse, the primers anneal within *Bin1* exon 10 (forward: 5′-TCAATGATGTCCTGGTCAGC-3′) and exon 12 (reverse: 5′-GCTCATGGTTCACTCTGATC-3′), PCR products are of 207 (+ exon 11) and 162 (– exon 11) bp.

BIN1 minigene construction and analysis. We PCR-amplified 229 nucleotides of upstream intron 10, BIN1 exon 11 and 220 nucleotides of downstream intron 11 (NT_022135.16) from human DNA (Clontech) and inserted the product between the HincII and BamHI restriction sites of the β-globin 4.11.12 vector (gift from T. Cooper). Next, the last 325 base pairs of intron 11 followed by BIN1 exon 12 were similarly amplified and inserted between the BamHI and NcoI restriction sites to replace the last β-globin exon. Mutations in BIN1 intron 11 were introduced by primer-directed PCR mutagenesis. C2C12 cells plated in six-well plates were co-transfected with Lipofectamine 2000 (Invitrogen) according to the manufacturer's instructions with *BIN1* minigene and DMPKS, DT960, GFP-CUGBP1 (NM_006560), GFP-MBNL1 40 kDa (NM_207292), siRNA (Eurogentec) directed against MBNL1 (5′-AACACGGAAUGUAAAU UUGCADTDT-3′) or against CUGBP1 (5′-GUUACGACAAUCCUGUUUCD TDT-3′) in DMEM medium containing 1 g l^{-1} glucose and 2% horse serum (37 °C, 5% CO_2) over 24 h. Total RNAs were extracted with Tri Reagent (Molecular Research Center) and subjected to reverse transcription by the Transcriptor Reverse Transcriptase kit (Roche). PCR was performed with Taq polymerase (Roche), one denturation step at 94 °C for 2 min, 25 cycles of amplification 94 °C for 1 min, 58 °C for 45 s, 72 °C for 1 min and a final step at 72 °C for 7 min using the forward primer 5′-CATTCACCACATTGGTGT GC-3′ and the reverse primer 5′-AAGTGATCCTAGACTAGCCGCC-3′ specific to the β-globin–*BIN1* minigene. The PCR products of mRNAs including and excluding exon 11 are of 345 and 300 bp, respectively. PCR products were precipitated, analyzed by eletrophoresis on a 6.5% polyacrylamide gel, stained with ethidium bromide and quantified with a Typhoon scanner.

Fluorescent *in situ* hybridization and immunofluorescence. The combined FISH–immunofluorescence experiment was done as described previously[22] with a Cy3-conjugated PNA (CAG)7x probe, a monoclonal mouse antibody to BIN1 (clone 99D directed against exon 17, Upstate, 1 in 200 dilution) and a secondary Alexa 488–conjugated goat antibody to mouse IgG (Invitrogen) or Cy3-conjugated donkey antibody to mouse IgG (Jackson ImmunoResearch). Other antibodies used were a monoclonal antibody to CACNA1S (DHPRα1 or CAV1.1) (mAB-1a, Chemicon, 1 in 100 dilution), polyclonal antibody to synemin (desmuslin) (gift from Z. Xue, 1 in 400), polyclonal antibody to desmin (Chemicon, 1 in 100), monoclonal antibody to ATP2A1 (clone IIH11, Abcam, 1 in 100), monoclonal antibody to RYR1 (clone 34C, Sigma, 1 in 100), monoclonal antibody to ACTN1 (clone SA20, Abnova) and polyclonal rabbit antibody to BIN1 (H100, SantaCruz, 1 in 100). Images were captured with a Leica confocal microscope and software (Leica Microsytems) and processed with Adobe Photoshop software.

***In vivo* gene transfer.** All mouse procedures were done according to protocol approved by the Committee on Animal Resources at the Centre d'Exploration Fonctionnelle of Pitie-Salpetriere animal facility and under appropriate biological containment. The U7-ex11AS construct and AAV production were done as previously described[28]. The tibialis anterior muscles of five male and six female newborns (10 d old) or adult female (2 months old) C57BL/6 mice were injected with respectively 10 or 50 µl of physiological solution containing the AAV2/1 vectors (1.8×10^{13} vector genomes per ml). For each mouse, one tibialis anterior muscle was injected with AAV (U7-ex11AS), and the contralateral muscle was injected with control AAV containing any transgene or vehicle alone (PBS). Four months after injections, mice were killed, muscles were collected and snap-frozen in liquid nitrogen–cooled isopentane and stored at –80 °C.

***In situ* force measurement.** The isometric contractile properties of tibialis anterior muscles (TA) were studied *in situ* as previously described[40] (Mouisel, E. *et al.*, 2006). Mice were anesthetized with pentobarbital (60 mg per kg body weight). The knee and foot were fixed with clamps and pins. The distal tendon of the tibialis anterior muscle was attached to a lever arm of a servomoteur system (305B, Dual-Mode Lever). Data were recorded and analyzed on a microcomputer using PowerLab system (4SP, ADInstruments) and software (Chart 4, ADInstruments). The sciatic nerve (proximally crushed) was stimulated by a bipolar silver electrode using a supramaximal (10-V) square wave pulse of 0.1 ms duration. Absolute maximal isometric tetanic force was measured during isometric contractions in response to electrical stimulation (frequency of 25 to 150 Hz, train of stimulation of 500 ms). Specific P0 was calculated by dividing P0 by muscle weight.

Additional methods. Detailed methodology is described in the **Supplementary Methods**.

40. Mouisel, E. *et al.* Outcome of acetylcholinesterase deficiency for neuromuscular functioning. *Neurosci. Res.* **55**, 389–396 (2006).

doi:10.1038/nm.2374

RESEARCH ARTICLE

Human Mutation

OFFICIAL JOURNAL
HGVS
HUMAN GENOME VARIATION SOCIETY
www.hgvs.org

A Mutation in a Rare Type of Intron in a Sodium-Channel Gene Results in Aberrant Splicing and Causes Myotonia

Tomoya Kubota,[1†] Xavier Roca,[2†] Takashi Kimura,[3] Yosuke Kokunai,[1] Ichizo Nishino,[4] Saburo Sakoda,[1‡] Adrian R. Krainer,[2] and Masanori P. Takahashi[1*]

[1]*Department of Neurology, Osaka University Graduate School of Medicine, Suita, Osaka, Japan;* [2]*Cold Spring Harbor Laboratory, Cold Spring Harbor, New York;* [3]*Division of Neurology, Department of Internal Medicine, Hyogo College of Medicine, Nishinomiya, Hyogo, Japan;* [4]*Department of Neuromuscular Research, National Institute of Neuroscience, National Center of Neurology and Psychiatry, Kodaira, Tokyo, Japan*

Communicated by Mario Tosi

Received 18 November 2010; accepted revised manuscript 25 February 2011.
Published online 15 March 2011 in Wiley Online Library (www.wiley.com/humanmutation). DOI 10.1002/humu.21501

ABSTRACT: Many mutations in the skeletal–muscle sodium-channel gene *SCN4A* have been associated with myotonia and/or periodic paralysis, but so far all of these mutations are located in exons. We found a patient with myotonia caused by a deletion/insertion located in intron 21 of *SCN4A*, which is an AT-AC type II intron. This is a rare class of introns that, despite having AT-AC boundaries, are spliced by the major or U2-type spliceosome. The patient's skeletal muscle expressed aberrantly spliced *SCN4A* mRNA isoforms generated by activation of cryptic splice sites. In addition, genetic suppression experiments using an *SCN4A* minigene showed that the mutant 5′ splice site has impaired binding to the U1 and U6 snRNPs, which are the cognate factors for recognition of U2-type 5′ splice sites. One of the aberrantly spliced isoforms encodes a channel with a 35-amino acid insertion in the cytoplasmic loop between domains III and IV of Nav1.4. The mutant channel exhibited a marked disruption of fast inactivation, and a simulation in silico showed that the channel defect is consistent with the patient's myotonic symptoms. This is the first report of a disease-associated mutation in an AT-AC type II intron, and also the first intronic mutation in a voltage-gated ion channel gene showing a gain-of-function defect.
Hum Mutat 32:773–782, 2011. © 2011 Wiley-Liss, Inc.

KEY WORDS: skeletal muscle; myotonia; splicing; gain of function; simulation; channelopathy

Introduction

Genetic defects in voltage-gated sodium channel (Nav) genes are responsible for several hereditary diseases [George, 2005]. Physiological studies of the mutant channels have revealed two types of functional defects, characterized by loss or reduction of conductivity (loss of function) or by altered gating (gain of function). Mutations in the skeletal–muscle sodium-channel gene *SCN4A* (MIM♯ 603967) are usually associated with myotonia and/or periodic paralysis and in a rare case with fatigable weakness (congenital myasthenia), and this type of disorder is inherited in an autosomal-dominant fashion [Cannon, 2006; Tsujino et al., 2003]. All of the identified mutations in *SCN4A* are located in the coding regions (exons), and the mutant Nav1.4 channels show gain-of-function defects, such as disruption of fast inactivation and/or enhancement of activation [Cannon, 2006]. To our knowledge, no mutations in *SCN4A* have been reported in noncoding regions (introns). Although disease-associated mutations located in noncoding regions have been identified in other voltage-gated ion channel genes, they generally show loss-of-function defects [Colding-Jorgensen, 2005; Dutzler et al., 2002; Ruan et al., 2009; Zimmer and Surber, 2008].

Pre-mRNA splicing relies on conserved, yet highly diverse sequence elements at both ends of introns, termed splice sites [Brow, 2002]. The vast majority of introns are bounded by GT-AG dinucleotides, and are usually recognized and spliced by the major or U2-type spliceosome, which comprises the U1, U2, U4, U5, and U6 small nuclear ribonucleoprotein particles (snRNPs) [Sheth et al., 2006]. In contrast, AT-AC introns are rare (0.34%) and usually spliced by the minor or U12-type spliceosome, comprising U11, U12, U4atac, U5, and U6atac snRNPs [Burge et al., 1998; Patel and Steitz, 2003; Sheth et al., 2006]. AT-AC introns occur frequently in voltage-gated ion channel genes, such as intron 2 and intron 21 in *SCN4A* [Wu and Krainer, 1996, 1997, 1999]. However, whereas intron 2 is spliced by the minor spliceosome, intron 21 is spliced by the major or U2-type spliceosome. Thus, intron 2 is classified as AT-AC type I, and intron 21 as AT-AC type II [Wu and Krainer, 1996, 1997]. Analogously, a small subset of GT-AG introns spliced by the minor spliceosome, further demonstrating that the terminal intronic dinucleotides do not hold enough information to determine their mechanism of recognition [Burge et al., 1998; Dietrich et al., 1997; Wu and Krainer, 1997]. A recent genomic study estimated only 15 AT-AC type II introns in the human genome (out of $\sim 2 \times 10^5$ introns), confirming that these introns are extremely rare [Sheth et al., 2006]. Furthermore, 10 out of the 15 AT-AC type II introns are found in

Additional Supporting Information may be found in the online version of this article.

[†]Contributed equally and should be considered joint first authors.

[‡]Present address: Department of Neurology, Toneyama Hospital, National Hospital Organization, Toyonaka, Osaka, Japan 5608552.

*Correspondence to: Masanori P. Takahashi, Department of Neurology, Osaka University Graduate School of Medicine, D4, 2-2, Yamadaoaka, Suita, Osaka 565-0871, Japan. E-mail: mtakahas@neurol.med.osaka-u.ac.jp

Contract grant sponsors: Intramural Research Grant for Neurological and Psychiatric Disorders of National Center of Neurology and Psychiatry 20B-13; Research Grants for Intractable Disease from the Ministry of Health Labour and Welfare; Grants-in-aid for Scientific Research from the JSPS; The Nakatomi Foundation (to M.P.T.); The National Institutes of Health; Contract grant number: GM42699 (to X.R. and A.R.K.).

members of the *Nav* channel gene family, and clearly have a common evolutionary origin [Wu and Krainer, 1997, 1999].

We found a patient with prominent myotonia caused by a deletion/insertion located in intron 21 of one of the *SCN4A* alleles. This is the first disease-associated mutation in the very rare class of AT-AC type II introns. The patient's skeletal muscle expressed aberrantly spliced *SCN4A* mRNA isoforms by activation of cryptic splice sites, and we observed the same aberrant splicing patterns when we tested mutant *SCN4A* minigenes. We further showed that the aberrantly spliced isoform encodes a channel with a 35-amino-acid insertion in the cytoplasmic loop, and this mutant channel exhibited a marked disruption of fast inactivation. In addition, we showed, using in silico simulation, that the defect of the channel is consistent with the patient's myotonic symptoms. This is the first case of a gain-of-function intronic mutation in a voltage-gated ion-channel gene.

Materials and Methods

Patient

The patient was a 35-year-old Japanese male with hypertrophic musculature (Fig. 1A). His family was not consanguineous and had no history of neuromuscular diseases. Due to myotonia, he had difficulties in opening his eyes and presented narrow palpebral fissures, which were exacerbated by repetitive contractions (eyelid paramyotonia). His distal extremities were atrophic and he had grade 2 muscle strength in the arms and grade 4 in the legs. Scoliosis was present and articular contractures were noted in shoulders, elbows, and wrists. Percussion myotonia in *abductor pollicis brevis* and *rectus abdominus* muscles and grip myotonia were present (Supp. Movies S1 and S2). Myotonia was exacerbated by cold exposure but not by intake of fruits. He also had difficulty in breathing, which probably was caused by myotonia of respiratory muscles. Administration of mexiletine alleviated his myotonic symptoms, including the difficulty in breathing. More detailed medical history is given in the Supporting Information.

Clinical Electrophysiological Examination

Clinical electrophysiological examinations were performed using Neuropack MEB 2216 (Nihon Kohden, Tokyo, Japan). In brief, needle electromyography was performed with *biceps brachii*, *extensor digitrum communis*, and *tibialis anterior* muscles using a concentric recording needle with a sampling frequency of 10 Hz–10 kHz. The compound muscle action potentials (CMAPs) of *abductor digiti minimi* were evoked by supramaximal stimulation of the ulnar nerve for 0.2 msec. The repeated short exercise test was performed as previously reported [Fournier et al., 2004, 2006].

Pathological Examination

After obtaining informed consent, a muscle specimen was extracted from the *gluteus maximus* muscle during surgery for a femur neck fracture. The specimens were snap frozen in isopentane cooled with dry ice, and stored at −80°C. Sections were stained with a battery of histochemical methods, including hematoxylin-eosin (H&E), ATPase (pH 10.2, pH 4.6, and pH 4.2) and acetylcholinesterase (AChE).

DNA Sequencing

We obtained informed consent from patients and family members enrolled in the study, using protocols approved by the

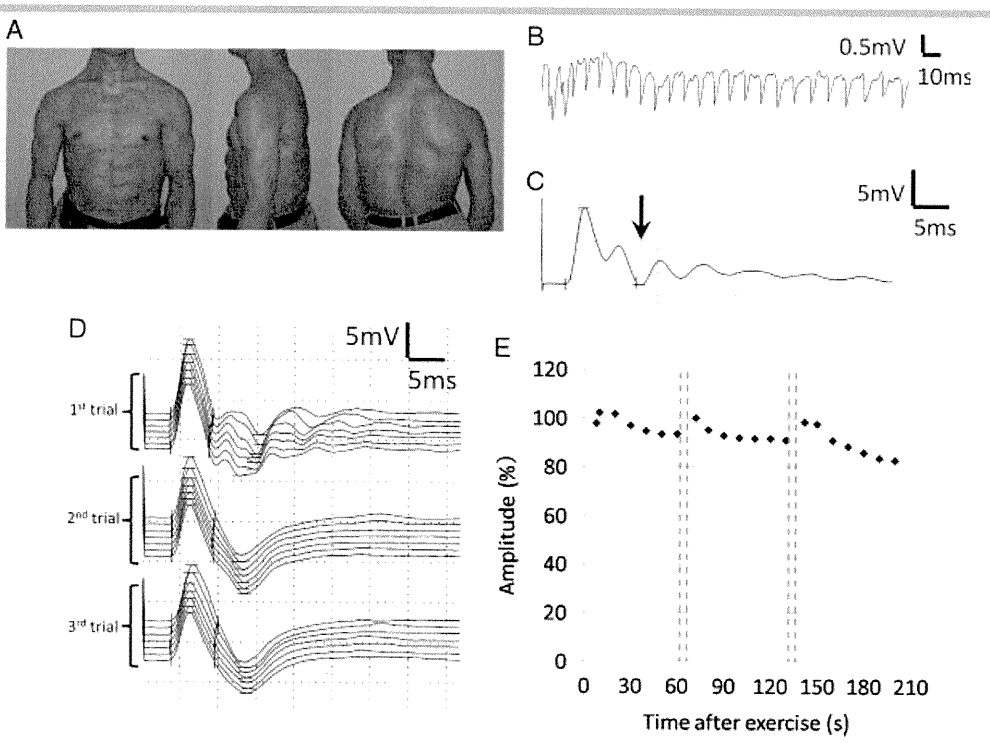

Figure 1. Clinical features of the patient. **A:** Images showing the hypertrophic upper body musculature of the patient. **B:** Needle electromyography recording of *tibialis anterior* muscle showed myotonic discharge. **C:** Compound muscle action potential (CMAP) recorded from *abductor digiti minimi* muscle showed postexercise myotonic potentials (PEMPs) (arrow). **D:** Traces of CMAP during the repeated short exercise test. PEMPs were observed in the first trial recording after 10-sec exercises, but disappeared with repeated exercises. **E:** A gradual decrease of the amplitude of CMAPs was observed with repeated short exercise.

Institutional Ethics Review Board at Osaka University. Genomic DNA was extracted from blood leukocytes from the patient and both parents. The regions encompassing all *SCN4A* (NM_000334.4) and *CLCN1* (NM_000083.2) exons were amplified by PCR (primer sequences and their location from the end of each exon are shown in Supp. Table S1), and the purified fragments were sequenced using an automated DNA sequencer (Big Dye Terminator v 3.1 and ABI310; PE Applied Biosystems, Foster City, CA). The PCR products including exon 21 and intron 21 were subcloned into the pCR2.1 TOPO vector (Invitrogen, Carlsbad, CA) and the nucleotide sequences of both alleles were determined. Nucleotide numbering reflects cDNA numbering with +1 corresponding to the A of the ATG translation initiation codon in the reference sequence, according to journal guidelines (www.hgvs.org/mutnomen). The translation initiation codon is codon 1.

mRNA Analysis

In addition to biopsied muscle from the patient, muscle specimens from myotonic dystrophy type 1 patients ($n = 3$) were used as disease controls. Total RNA was extracted from each sample using ISOGEN (Nippon Gene, Tokyo, Japan). First-strand cDNAs were synthesized from 1.8 μg of total RNA using random hexamers, and the cDNAs were amplified by 35 cycles of PCR (primer sequences in Supporting Information). The sizes of the PCR products were analyzed by agarose-gel electrophoresis stained with ethidium bromide, and the fluorescent intensity of each band was quantified using FluoroImager (GE Healthcare, Fairfield, CT). The RT-PCR products were cloned into the pCR2.1 TOPO vector, and the plasmids were transformed into competent *Escherichia coli* (ECOS^{TM} Competent E. Coli XL1-Blue, Nipongene, Tokyo, Japan). A total of 42 colonies were purified and sequenced.

Minigene Construction and Transient Transfection

The genomic fragment encompassing *SCN4A* exon 20 to exon 22 was amplified using the patient's genomic DNA (primer sequences in Supporting Information). Purified wild-type and mutant PCR fragments were cloned into the mammalian expression vector pcDNA3.1+ (Invitrogen). Clones were sequenced to exclude the presence of additional mutations.

U1 and U6 expression plasmids are described elsewhere [Roca and Krainer, 2009]. Mutations at the 5′ end of U1 or at the conserved U6 ACAGAG box were introduced by site-directed mutagenesis. All constructs were verified by sequencing.

HeLa cells were cultured in DMEM (Invitrogen) containing 10% (v/v) fetal bovine serum (FBS) and antibiotics (100 U ml^{-1} penicillin and 100 μg ml^{-1} streptomycin). We mixed 80 ng of the *SCN4A* minigenes with 400 or 800 ng of the U1 and U6 plasmids, and with 80 ng of the pEGFP-N1 plasmid (Clontech, Palo Alto, CA). HeLa cells were transfected with the plasmid mixes using FuGENE 6 (Roche Diagnostics, Indianapolis, IN) as previously reported [Roca and Krainer, 2009]. RNA was harvested 48 hr after transfection using TRIzol (Invitrogen). Residual DNA was eliminated with RQ1-DNase (Promega, Masdison, WI), and the RNA was recovered by phenol extraction and ethanol precipitation. A total of 1 μg of RNA was used for reverse transcription with Superscript II RT (Invitrogen) and oligo-dT as a primer.

The minigene cDNAs were amplified by PCR using primers located in the transcribed portion of the pcDNA3.1+ plasmid [Roca and Krainer, 2009]. The 5′ end of one of the PCR primers was radiolabeled using T4 polynucleotide kinase (New England Biolabs, Beverly, MA) and γ-^{32}P-ATP, and the primer was purified using MicroSpin G-25 columns (GE Healthcare). A total of 23 cycles of PCR were performed to ensure that amplification remained in the exponential phase. The PCR products were separated by 6% native PAGE, and the gels were exposed on BioMAX XAR film (Kodak, Rochester, NY). The identity of each band was determined by cloning of separate nonradioactive RT-PCR products into the Original TA Cloning kit (Invitrogen) followed by sequencing on an ABI3730 automated sequencer.

Construction of Expression Vector for the Aberrantly Spliced Isoform

Polymerase chain reaction (PCR) of the patient's cDNA was performed using primers shown in the Supporting Information. An Sse83871 (TaKaRa, Japan)-digested fragment of the PCR product was cloned into a mammalian expression construct for the human skeletal muscle sodium channel, pRc/CMV-hSkM1 [Takahashi and Cannon, 1999].

Na-Current Recording Using Cultured Cells

Cultures of human embryonic kidney (HEK) 293T cells and their transient transfection were performed as described [Green et al., 1998; Takahashi and Cannon, 1999]. In brief, plasmid cDNAs that encoded wild-type (0.8 μg/35-mm dish) or mutant human Na channel α-subunits (1.6 μg/35-mm dish), the human Na channel β-subunit (fourfold molar excess over α-subunit DNA), and a CD8 marker (0.1 μg/35-mm dish) were used to cotransfect HEK-293T cells by the calcium phosphate method. Transfection-positive cells are identified by attachment of CD8 antibody-coated beads (Dynal, Oslo Norway).

For measuring the current density, the same amount of α-subunit plasmids (1.6 μg/35-mm dish) were used for both wild-type and mutant channels. For the kinetic analyses, the amount of wild-type plasmid for transfection was reduced to one half of that of the mutant channel, because of the higher expression level of the wild-type channel.

At 2–3 days after transfection, we measured sodium currents using conventional whole-cell recording techniques with an Axopatch 200B amplifier (Molecular Devices, Sunnyvale, CA). Any cells with peak currents of <0.5 or >15 nA on step depolarization from −120 to −10 mV were discarded. The pipette (internal) solution consisted of: 105 mM CsF, 35 mM NaCl, 10 mM EGTA, and 10 mM Cs-HEPES (pH 7.4). The bath solution consisted of: 140 mM NaCl, 4 mM KCl, 2 mM $CaCl_2$, 1 mM $MgCl_2$, 5 mM glucose, and 10 mM Na-HEPES (pH 7.4).

The current density (pA/pF) was calculated using the capacitance of each cell and the peak current elicited by a depolarization pulse of −10 mV from a holding potential of −120 mV. The voltage dependence of steady-state fast inactivation was measured as the peak current elicited after a 300-msec conditioning pulse from a holding potential of −120 mV. The voltage dependence of steady-state slow inactivation was measured as the peak current elicited by the test pulse after a 60-sec conditioning prepulse, followed by a 20-msec gap at −120 mV to allow recovery from fast inactivation. The kinetics of the fast inactivation was characterized by measuring the voltage dependence of the time constant using three different protocols: (1) the current decay in the depolarized range; (2) the entry protocol in the

intermediate ranges; and (3) the recovery protocol in the hyperpolarized range.

Data Analysis

Curve fitting was manually performed off-line using Origin (Microcal LLC, Northampton, MA). Conductance was calculated as $G_{(V)} = I_{peak\,(V)}/(V - E_{rev})$, where the reversal potential, E_{rev}, was measured experimentally for each cell. The voltage dependence of activation was quantified by fitting the conductance measures to a Boltzmann function as $G_{(V)} = G_{max}/[1+\exp(-(V-V_{1/2})/k)]$. Steady-state fast inactivation was fitted to a Boltzmann function calculated as $I/I_{max} = 1/[1+\exp((V-V_{1/2})/k)]$, where $V_{1/2}$ was the half-maximum voltage and k was the slope factor. Steady-state slow inactivation was fitted to a Boltzmann function with the nonzero pedestal (S_0). Symbols with error bars indicate the mean ± standard error of the mean (SEM). Statistical significance was determined using an unpaired t-test with Origin.

Simulation

Computer simulations of skeletal muscle were performed using the model previously reported by Cannon et al. [1993], with minor modifications. The model included potassium and sodium channels described with the Hodgkin-Huxley model and leak-current on the two electrically connected compartments (cell surface and the membrane of T-tubule system). We coded the model with Excel Visual Basic Application (Microsoft, Redmond, WA). Parameter values used for the wild type were identical with those reported previously [Hayward et al., 1996]. Parameters for fast inactivation of the mutant channel were estimated from the fit of experimental data with a two-state model.

Results

Clinical Electrophysiology and Muscle Histopathology

The patient was evaluated with clinical electrophysiological-methods. Myotonic discharges were present in all muscles examined by needle electromyography (Fig. 1B). The repeated short exercise test was performed to discriminate between myotonia caused by either Na or Cl channel mutations. After short exercises, abnormal sustained responses following the initial compound muscle action potential (CMAP) were observed, which were previously reported as postexercise myotonic potentials (PEMPs) (Fig. 1C) [Fournier et al., 2004, 2006]. During the repeated short exercise test, PEMPs disappeared (Fig. 1D) and the amplitude of CMAP decreased gradually (Fig. 1E). The observed postexercise decrease of electrical muscle response at room temperature was suggestive of myotonia caused by a Na-channel mutation.

Pathological examination of the biopsied muscle showed a myopathic change with marked variation in fiber size. Hypertrophic fibers with multiple internal nuclei were abundant. Type 1 fiber predominance and type 2B fiber deficiency were seen upon myosin ATPase staining (Supp. Fig. S1A–D). Acetylcholinesterase (AchE) activity was increased in the sarcolemma (Supp. Fig. S1E).

Analysis of Genomic DNA and mRNA Splicing Isoforms

Nucleotide sequence analysis of the patient's DNA showed no mutation in any exons of *SCN4A* and *CLCN1*. On electropherogram, however, two overlapping traces were consistently observed, starting from the sixth nucleotide downstream from the boundary between exon 21 and intron 21 of *SCN4A* (Supp. Fig. S2A). To analyze the sequences of each strand, the PCR products encompassing exon 21 and intron 21 were subcloned into the pCR2.1 TOPO vector. Sequence analysis of each strand revealed a heterozygous mutation in intron 21, which consists of a five-nucleotide deletion and one-nucleotide insertion at the sixth nucleotide downstream from the boundary between exon 21 and intron 21 (NG_011699.1:c.3912+6_3912+10delinsG) (Fig. 2A). Neither his parents nor 220 normal alleles harbored this mutation (Supp. Fig. S2A).

Because this mutation affects a portion of the 5′ splice site, we hypothesized that it might influence the splicing of intron 21. To examine the splicing patterns of the mutant transcript, RT-PCR was performed using mRNA extracted from skeletal muscle. In control muscles, only a fragment with the expected size (325 nucleotides) was observed. In muscle from the patient, however, two additional fragments were observed: one larger and the other smaller than normal. By measuring the fluorescent intensity of these bands, the proportion of each isoform was estimated as follows: large isoform: 33%; normal isoform: 57%; small isoform: 10% (Fig. 2B). To determine the nucleotide sequence, RT-PCR products were subcloned into the pCR2.1 TOPO vector. Sequence analysis showed that the smaller fragments consisted of two isoforms: one originated by splicing between a cryptic 5′ splice site in exon 21 and a cryptic 3′ splice site located at the initial portion of exon 22 (Deletion type: 2/42 colonies); the other one as a result of splicing from the 5′ splice site of exon 20 to the same cryptic 3′ splice site of exon 22 (Skip type: 8/42 colonies). Both small isoforms are predicted to be translated out of frame, with their reading frames interrupted by premature termination codons. The large isoform resulted from splicing between a cryptic 5′ splice site in intron 21 and the same cryptic 3′ splice site as above (retention type: 4/42 colonies). This isoform is in frame (Fig. 2C), and is predicted to encode a channel with a one-amino acid deletion and 35-amino acid insertion in the DIII-DIV linker of Nav1.4, which could retain some degree of functionality (Fig. 2D and Supp. Fig. S2B). It should also be noted that the AT-AC type II intron 21 was replaced with aberrant GT-AG introns in all the abnormal isoforms (Supp. Fig. S3).

Minigene Analysis Confirms the Molecular Diagnosis of the SCN4A Mutation

The deletion/insertion (TATCA>G) in intron 21 of one of the *SCN4A* alleles was a candidate mutation to cause the splicing defects associated with the patient's myotonia. This mutation affects position +6 (the sixth intronic nucleotide) of the 5′ splice site, which is one of the less conserved positions of GT-AG U2-type 5′ splice sites. In addition, the mutation also changes positions +7 and +8, which are not conserved at all in this class of 5′ splice sites. Nevertheless, these nucleotide changes at positions +6 to +8 reduce the base-pairing potential to the 5′ end of the U1 snRNA (Fig. 3A), which is an early essential interaction for 5′-splice-site selection in U2-type introns [Seraphin et al., 1988; Siliciano and Guthrie, 1988; Zhuang and Weiner, 1986]. In addition, the mutation also disrupts base-pairing to the conserved ACAGAG box in U6 snRNA (Fig. 3D), which replaces U1 later in spliceosome assembly [Kandels-Lewis and Seraphin, 1993; Lesser and Guthrie, 1993; Wassarman and Steitz, 1992]. In any case, because this is the first disease-associated 5′-splice-site mutation in an AT-AC type II intron,

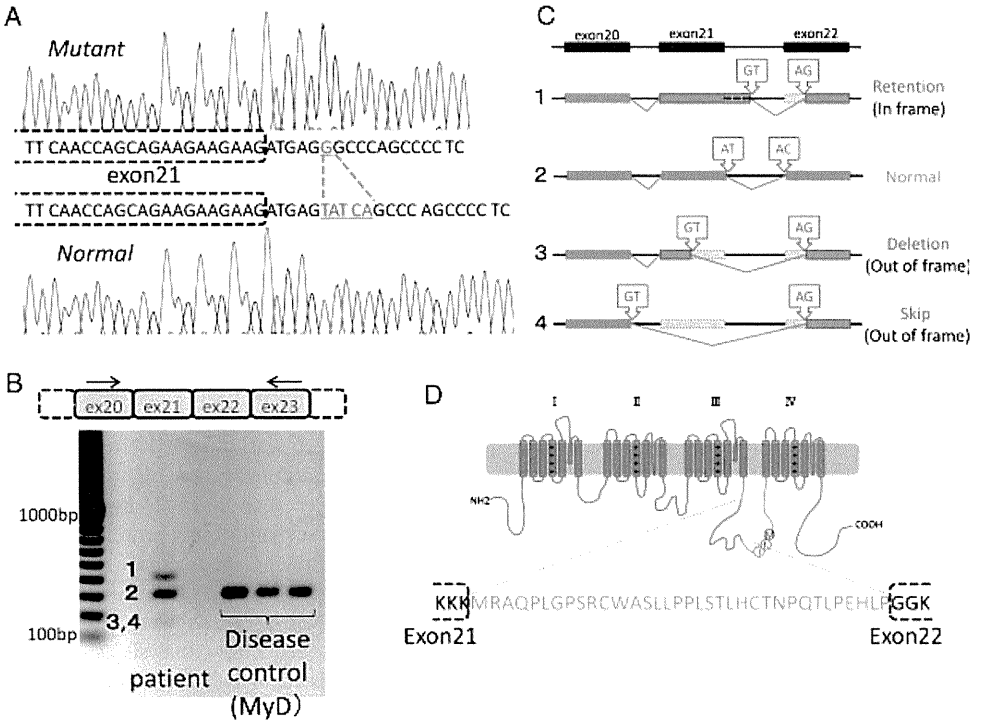

Figure 2. Genomic DNA and mRNA analysis. **A:** Both alleles of the patient's genomic DNA sequences around the boundary between exon 21 and intron 21 of *SCN4A* are separately shown. Deletion of five nucleotides (TATCA) and insertion of one nucleotide (*G*) were observed in one allele (c.3912+6_3912+10delinsG). **B:** RT-PCR from patient muscle mRNA revealed several aberrantly spliced isoforms, in addition to the normal isoform expressed in the disease control. Numbered bands (1–4) correspond to the isoforms in Figures 2C and 3C. Arrows indicate the primers used for RT-PCR. **C:** Summary of the sequence analysis of all isoforms. Lines indicate introns, and dark blue or red boxes indicate normal or aberrant exons, respectively. Light blue boxes indicate portions of the normal exons that were removed in the aberrant isoforms. Arrowhead rectangles indicate the splice-site dinucleotides. **D:** Schematic illustration of the mutant Nav 1.4 channel α subunit. The in-frame isoform encodes a large insertion (amino acids in blue type) in the domain III and IV linker.

additional evidence was necessary to unambiguously determine the pathogenicity of this mutation.

We transiently transfected HeLa cells with the wild-type and mutant *SCN4A* minigenes, and analyzed the splicing patterns by radioactive RT-PCR, as well as by cloning and sequencing to confirm the identity of the PCR products. Both *SCN4A* minigenes recapitulated the splicing patterns seen in either control or patient cells, respectively (Fig. 3B and C). The wild-type *SCN4A* minigene showed efficient splicing at the AT-AC type II boundaries, with traces of exon 21 skipping and activation of the cryptic GT-AG splice sites (Fig. 3C, lane 1). In contrast, the mutant minigene showed no splicing at the AT-AC splice sites, but gave rise to the same three aberrantly spliced isoforms seen in patient cells. These results confirmed the molecular diagnosis of the *SCN4A* intron 21 TATCA>G mutation as the cause of the patient's myotonia (Fig. 3C, lane 2).

The SCN4A Mutation Disrupts Base-Pairing to U1 and U6 snRNAs

We used genetic suppression analyses to investigate the molecular mechanisms underlying defective splicing due to the mutation at the AT-AC type II 5′ splice site in *SCN4A*. We cotransfected cells with the *SCN4A* mutant minigene with suppressor U1 and/or U6 snRNAs carrying compensatory mutations that restore base-pairing to the mutant 5′ splice site [Cohen et al., 1994; Mount and Anderson, 2000; Roca and Krainer, 2009; Seraphin et al., 1988; Siliciano and Guthrie, 1988; Zhuang and Weiner, 1986]. None of the multiple suppressor U1s carrying one or several compensatory mutations could rescue correct splicing at the AT-AC boundaries (Fig. 3C, lanes 3–8). In previous U1-suppressor experiments for U2-type GT-AG 5′ splice sites, restoring base-pairing to U1 snRNA alone was sufficient to rescue correct splicing [Roca and Krainer, 2009; Seraphin et al., 1988; Siliciano and Guthrie, 1988; Zhuang and Weiner, 1986], suggesting that the mutation at the *SCN4A* AT-AC type II 5′ splice site critically affects other recognition steps. The U6 suppressors alone could not rescue correct AT-AC splicing either (Fig. 3E, lane 3, and data not shown), in contrast to what was previously seen with mutant U2-type GT-AG 5′ splice sites [Carmel et al., 2004; Roca and Krainer, 2009]. Interestingly, combining certain suppressor U1 and U6 snRNAs rescued splicing via the AT-AC splice sites, albeit weakly (Fig. 3E, lane 6). This weak restoration of correct splicing could not be augmented by using different combinations of U1 and U6 suppressors, or by introducing additional compensatory mutations in U6 (Fig. 3E, lane 7, and data not shown). In some cases, a cryptic GT-AG splice-site pair was activated (Fig. 3C, lane 5, and Fig. 3E, lanes 6 and 7), for unknown reasons. Taken together, these results suggest that the *SCN4A* intron 21 TATCA>G mutation disrupts optimal base-pairing to both U1 and U6 snRNAs.

Current Density and Gating of the Mutant Channel

We examined the functional consequences of this aberrant splicing by recording whole-cell Na currents from HEK-293T cells transiently transfected with the mutant Na channel cDNA. The

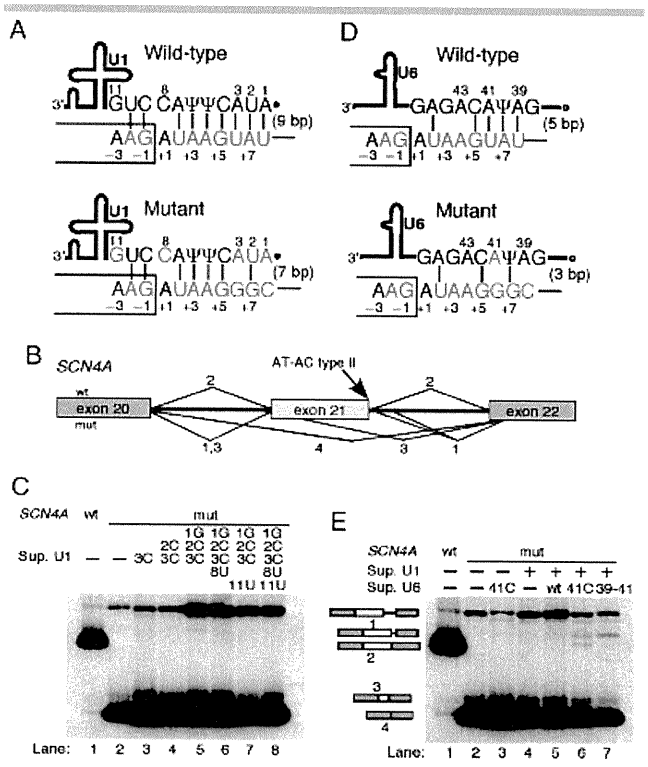

Figure 3. Mechanism of pathogenicity for the AT-AC type II intron mutation. **A:** Schematic of the base-pairing between the wild-type and mutant *SCN4A* intron 21 5′ splice site and the 5′ end of U1 snRNA. Thick line, U1 snRNA body; filled dot, trimethyl-guanosine cap; Ψ, pseudouridine. The box and the line depict portions of the exon and intron, respectively. Consensus and mutant nucleotides are shown in red and green, respectively. Nucleotides that were mutated in suppressor U1 snRNAs are shownin blue. The nucleotide positions at the 5′ splice site and at the 5′ end of U1 are numbered. Base pairs are depicted as vertical lines, and the total number is indicated in parenthesis. **B:** Schematic of the normal and aberrantly spliced isoforms shown in panel C. Isoforms are numbered as in Figure 2. The location of the AT-AC type II 5′ splice site is indicated. **C:** Suppressor U1 snRNAs alone could not rescue splicing at the mutant 5′ splice site. The *SCN4A* minigene and suppressor U1 used are indicated above the autoradiograms. The various mRNAs are indicated on the right, and correspond to those seen in patient cells (Fig. 2C). **D:** Schematic of the base pairing between the wild-type and mutant 5′ splice site and the conserved ACAGAG box of U6 snRNA. Open circle, γ-monomethyl cap. Font colors as in **A**. **E:** Suppressor U1 and U6 snRNAs partially rescue splicing at the mutant AT-AC type II 5′ splice site. The various constructs are indicated above the autoradiogram, and the identity of the mRNAs on the left. The U1 suppressor used was 1G2C3C, which together with the U6 suppressor 41C restored some correct splicing (lane 6).

current density of the mutant channel was approximately half that of the wild type (Fig. 4A).

Figure 4B shows normalized macroscopic Na currents of both wild-type and mutant channels, which were elicited by a depolarization pulse of −10 mV from a holding potential of −120 mV. The mutant channel current decayed more slowly than that of wild type, suggesting disruption of fast inactivation. The voltage dependence of steady-state fast inactivation measured with 300-msec conditioning pulse was shown in Figure 4A. The midpoint of the steady-state fast-inactivation curve for the mutant channel was shifted in the direction of depolarization by 19.1 mV compared to that of the wild type. The estimated parameters of steady-state fast inactivation were as follows: wild type: $V_{1/2} = -70.4 \pm 1.4$ ($n = 14$), $k = 5.0 \pm 0.2$ ($n = 14$); mutant: $V_{1/2} = -51.3 \pm 1.0$ ($n = 35$), $k = 7.0 \pm 0.2$ ($n = 35$) (Table 1). On the other hand, the voltage dependence of the mutant channel conductance was not different from that of the wild type (Fig. 4C and Table 1).

The voltage dependence of steady-state slow inactivation measured using a 60-sec conditioning prepulse was shown in Figure 4D. The midpoint of the steady-state slow inactivation curve for the mutant channel was shifted in the direction of depolarization by 8.1 mV compared to that of the wild type. The slope factor for the mutant channel was steeper than that of the wild type. However, the maximum extent of slow inactivation (S_0) did not differ between the wild-type and mutant channels (Table 1).

The kinetics of the fast inactivation was characterized by measuring the voltage dependence of the time constant using three different protocols. The time constants were analyzed by a single-exponential fit (see Supp. Fig. S4 for the analysis by two-exponential fit), in order to estimate the parameters of a two-state model, which are suitable for a simulation based on the Hodgkin-Huxley model. For the mutant channel, the voltage dependence of time constants was shifted in the direction of depolarization, and the time constants at the depolarized range were significantly slower (Supp. Fig. S5). Subsequently, the forward and backward rates of two-state model were estimated from the voltage dependence of steady-state fast inactivation and the time constants. For the mutant channel, the estimated value for the forward rate (α) was approximately four times and the backward rate (β) was one-fifth of those for wild type. The detail of the analysis is described in the Supporting Information.

Computer Simulation

Although the depolarized shift of steady-state fast-inactivation curve was consistent with enhanced membrane excitability, a computer simulation was performed to examine whether the functional defects of the mutant channel can recapitulate the symptoms, especially because the expression levels of the mutant channel could not be measured. The simulation based on the Hodgkin-Huxley model—which was previously reported by Cannon et al. [1993]—was reconstructed with Visual Basic. All the gating parameters for the wild-type channel were the same as those previously reported by Hayward et al. [1996] (Supp. Table S2). The parameters for fast inactivation of the mutant channel were modified based on the result in Supp. Figure S5. The fraction of the persistent current (f) for the mutant channel was estimated by averaging the currents in the last 5 msec of the 300-msec depolarization. All the other parameters for the mutant channel were identical to those for the wild type. The stimulating current was applied as a square wave (100 mA, 150 msec). Because the expression of the mutant channel is likely lower than that of the wild type, simulation studies were performed varying the proportion of the mutant channel. When the expressed Na channel was all wild type, repetitive firing of action potentials was not seen (data not shown). When the expression of the mutant channel was set at 50% of the total Na channel, repetitive firing of action potentials was observed (Fig. 5A). When the expression of the mutant channel was set at 35%, repetitive firing of action potentials was still evoked (Fig. 5B). Moreover, in the case of decreasing the expression of the mutant channel to 15%, repetitive firing of action potentials was still observed, although the degree of firing was not as robust (Fig. 5C). Overall, the results of this simulation suggest that the functional defect of the channel is sufficient to cause myotonia, even when the

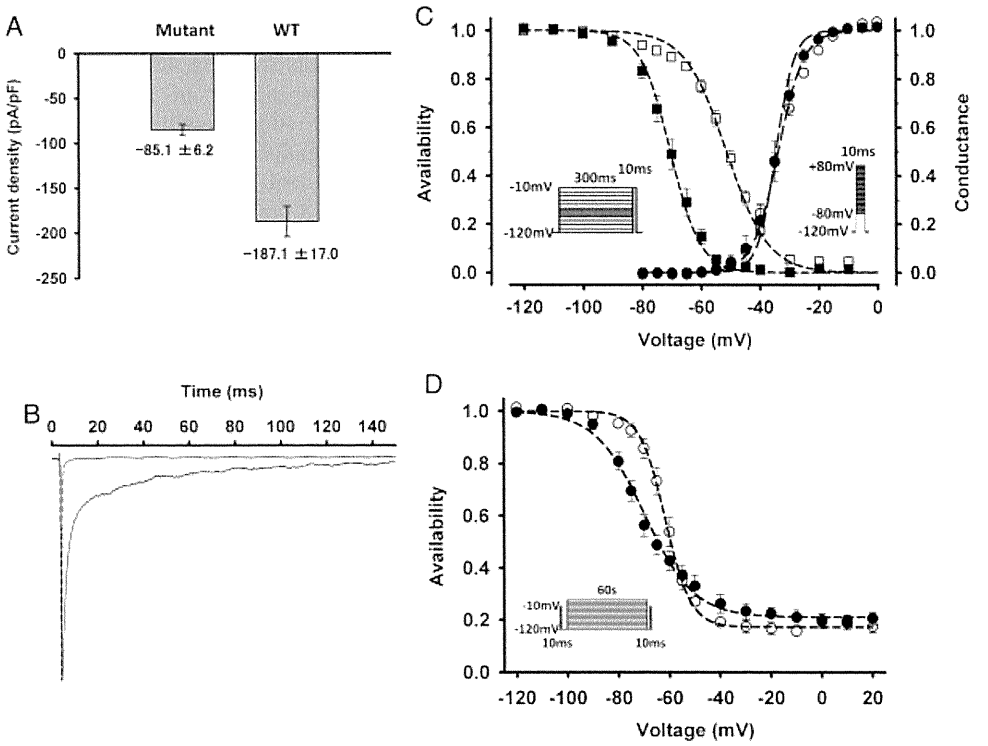

Figure 4. Current density and gating of the mutant channel. **A:** The current density (pA/pF) of the mutant channel ($n = 39$) is approximately half that of wild type ($n = 9$) when the same amount of the corresponding expression plasmids was used for transfection. Error bars indicate SEM. **B:** Normalized macroscopic sodium current elicited by a depolarization pulse of −10 mV from a holding potential of −120 mV. The mutant channel (solid line) showed slower decay than the wild type (dotted line), suggesting a disruption of fast inactivation. **C:** Voltage dependence of availability (steady-state fast inactivation, left, squares) and conductance (activation, right, circles). Filled and open symbols represent the wild-type and mutant channels, respectively. The midpoint of the steady-state fast inactivation curve for the mutant channel ($V_{1/2}$) was shifted in the direction of depolarization by 19.1 mV, compared to that for the wild type. The insets show the protocols used to measure the voltage dependence of steady-state fast inactivation (left) and the conductance (right). **D:** The voltage dependence of steady-state slow inactivation for the wild-type channel (filled symbols) and mutant channel (open symbols). The maximum extent of slow inactivation does not differ between the wild-type and mutant channels. The inset shows the protocol.

Table 1. Parameter Estimates for Wild-Type and Mutant Channels

	Activation		Fast inactivation		Slow inactivation		
	$V_{1/2}$ (mV)	k (mV/e-fold)	$V_{1/2}$ (mV)	k (mV/e-fold)	$V_{1/2}$ (mV)	k (mV/e-fold)	S_0
WT	−34.6±1.5 (14)	3.1±0.3* (14)	−70.4±1.4* (14)	5.0±0.2* (14)	−69.7±1.8* (9)	9.6±0.7* (9)	0.21±0.02 (9)
Mutant	−33.8±0.7 (35)	4.4±0.2* (35)	−51.3±1.0* (35)	7.0±0.2* (35)	−61.6±1.7* (7)	4.9±0.3* (7)	0.17±0.02 (7)

$V_{1/2}$ is the midpoint value of the steady-state inactivation curve and the voltage dependence of the conductance curve. k is the slope factor. S_0 is the nonzero pedestal. Values are means±SEM. *$P<0.01$.

expression of the mutant channel is as low as 15% of the total SCN4A channel.

Discussion

We have identified a causative mutation located in intron 21 of *SCN4A* in a patient with myotonia. The patient's myotonia was confirmed by needle electromyography, and was exacerbated by cold exposure and repetitive exercise (paramyotonia). Neurophysiological tests showed PEMPs and the characteristic decreasing of CMAPs with repeated short exercises [Fournier et al., 2004, 2006]. The clinical features and the results of the neurophysiological tests are consistent with myotonia due to a defect in Nav1.4. Hereditary skeletal–muscle diseases caused by mutations in *SCN4A* have been classified into paramyotonia congenita (PMC; MIM# 168300), potassium-aggravated myotonia (PAM; MIM# 608390), and hyperkalemic periodic paralysis (HyperPP; MIM# 170500) [Cannon, 2006]. Furthermore, the most severe form of PAM is called *myotonia permanens*, for which the only causative mutation reported to date is G1306E [Lehmann-Horn et al., 1990]. As the patient showed prominent generalized myotonia, associated with difficulty in breathing, hypertrophic musculature, joint contractures, and scoliosis, we assumed that his clinical features were indicative of *myotonia permanens*. Although he presented myotonia exacerbated by cold exposure, and paramyotonia in the eyelids, two symptoms characteristic of PMC rather than PAM, several cases of PAM exacerbated by cold exposure have been reported. As mentioned above, classification of sodium-channel myotonic disorders is sometimes difficult, because of their clinical overlap. Recently, the Consortium of Clinical Investigators of Neurological Channelopathies has proposed that sodium-channel myotonic disorders might be simply classified into two

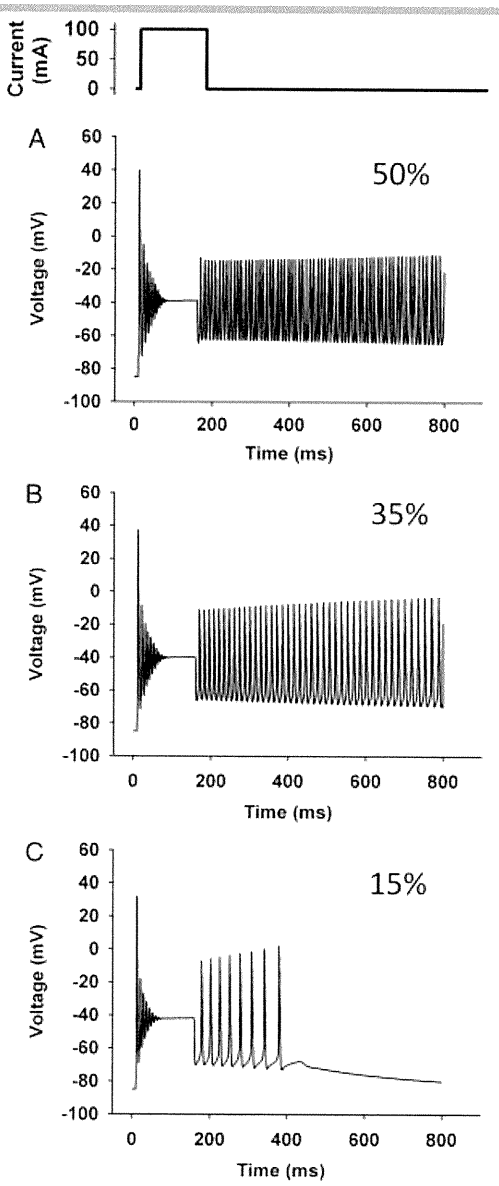

Figure 5. Computer simulation. The upper inset indicates the stimulating current (100 mA, 150 msec). The simulation was performed by varying the proportion of the mutant channel, because the expression of the mutant channel in the patient's muscle is unknown (**A**: 50%; **B**: 35%; **C**: 15%). Repetitive firing of action potentials was observed even when expression of the mutant channel was set at 15%.

broad groups, based on the presence or absence of episodic weakness: PMC or sodium-channel myotonia, respectively [Matthews et al., 2010]. According to this proposal, our case might be classified into sodium-channel myotonia, because of the lack of clear episodic weakness. Another clinical feature of interest is muscle atrophy in distal upper extremities. However, this would not exclude nondystrophic myotonia. In fact, dystrophic features have been reported in myotonia caused by Na-channel and Cl-channel mutations [Kubota et al., 2009; Nagamitsu et al., 2000; Plassart et al., 1996; Schoser et al., 2007].

From a clinicogenetic point of view, this mutation is unprecedented in two ways. First, this is the first disease-associated intronic mutation in a voltage-gated ion channel gene showing a gain-of-function defect. Many different mutations in voltage-gated ion channel genes have been identified as causes for inherited disorders, but these mutations mostly map to the coding exons [Cannon, 2006; George, 2005]. A few disease-associated mutations in noncoding regions of voltage-gated ion channel genes have been reported. For example, at least six mutations associated with autosomal-recessive (Becker) myotonia congenita have been identified in noncoding regions of the skeletal–muscle chloride-channel gene, *CLCN1* [Colding-Jorgensen, 2005]. Similarly, at least seven mutations causing Brugada syndrome have been identified in the noncoding regions of the cardiac muscle sodium-channel gene *SCN5A* [Ruan et al., 2009; Zimmer and Surber, 2008]. Notably, mutant channels causing Becker-type myotonia congenita and Brugada syndrome generally exhibit loss-of-function defects. Moreover, a splice-site mutation in the neuronal sodium channel *SCN1A* was identified in a patient with partial epilepsy with febrile seizures, although the properties of the mutant channel have not been assessed [Kumakura et al., 2009]. Here we described a heterozygous mutation in a non-coding region of *SCN4A* that causes aberrant splicing. Our results strongly suggest that one of the aberrantly spliced mRNA isoforms is translated into a functional channel that displays a gain-of-function defect. Therefore, our case constitutes a novel mechanism of pathogenesis for inherited channelopathies.

Second, the deletion/insertion in intron 21 of *SCN4A* is the first disease-associated mutation identified in a very rare class of introns, known as AT-AC type II. An intronic mutation in the other, more common type of AT-AC intron (AT-AC type I, or U12-dependent) in the *LKB1* gene was found to cause Peutz-Jeghers syndrome [Hastings et al., 2005]. No disease-associated mutation in AT-AC type II introns had been described until now, probably because of the very low number (only 15) of such introns in the human genome [Sheth et al., 2006]. Because 10 out of 15 AT-AC type II introns are found in members of Nav-channel gene family, other mutations in these introns may be found to be associated with channelopathies in the future.

The splicing defects caused by the *SCN4A* intron 21 mutation were confirmed by minigene analysis. The splicing patterns from the wild-type and mutant *SCN4A* minigenes faithfully matched those seen in control and patient cells, respectively. The disruption of the AT 5′ splice site resulted in aberrantly spliced mRNAs by activation of cryptic GT-AG pairs. This observation is consistent with the notion that AT 5′ splice sites are almost exclusively paired with AC 3′ splice sites [Dietrich et al., 1997; Parker and Siliciano, 1993; Sheth et al., 2006; Wu and Krainer, 1997].

Our genetic suppression experiments provided a mechanistic basis for the pathogenic effect of the deletion/insertion in intron 21. These tests suggested that the mutant AT-AC type II 5′ splice site is defective in efficient base-pairing to both U1 and U6 snRNAs, which are key splicing factors that sequentially bind U2-type 5′ splice sites. This might constitute a fundamental difference between AT-AC type II and GT-AG 5′ splice sites, in that 5′ splice-site mutations in GT-AG introns can usually be rescued by suppressor U1s alone [Roca and Krainer, 2009; Seraphin et al., 1988; Siliciano and Guthrie, 1988; Zhuang and Weiner, 1986], whereas in this case we only observed weak rescue when both U1 and U6 suppressors were expressed simultaneously. Further U1/U6 suppressor analysis using other AT-AC type II introns is needed to confirm the generality of the U6 dependence of *SCN4A* AT-AC type II introns.

Interestingly, the AT-AC type II mutation results in activation of cryptic U2-type GT-AG splice-site pairs, similarly to what was seen upon mutations in minor-spliceosome or U12-type introns [Hastings et al., 2005; Incorvaia and Padgett, 1998; Kolossova and Padgett, 1997]. These cryptic GT-AG pairs are present in the

wild-type pre-mRNA, but remain silent unless one of the AT-AC splice sites is mutated. Whereas GT-AG U2-type splice sites exhibit a very high degree of variation, with thousands of different sequences acting as functional splice sites in the human genome [Roca and Krainer, 2009], U12-type splicing elements (specifically the 5′ splice site and the branch point sequence) are very highly conserved, suggesting that these sequences are constrained to be functional [Sheth et al., 2006]. Our observations suggest that AT-AC type II introns are similarly constrained, and that one of these constraints might be the need for efficient base-pairing to U6 snRNA, possibly because of the G>A difference at the first intronic position. It remains possible that there are specific splicing elements and factors required for efficient splicing of AT-AC type II introns, but these are not identifiable by genomic analyses because of the very low number of such introns. In short, mutations that disrupt AT-AC type II splice sites, like those affecting U12-type splice sites, result in activation of cryptic U2-type GT-AG splice sites, because the sequence requirements for these U2-type GT-AG splice sites are much more flexible.

The functional properties of the aberrantly spliced channel provide further understanding about the molecular mechanism of fast inactivation of the sodium channel. It has been established that the DIII-DIV linker plays a key role in fast inactivation of sodium channels. In particular, a cluster of hydrophobic amino acids (IFM) in the DIII-DIV linker is believed to function as an essential component of the fast inactivation particle, which occludes the intracellular mouth of the activated channel by a " ball-and-chain" or "hinged-lid" mechanism [Armstrong and Bezanilla, 1977; West et al., 1992]. In Nav1.4, the DIII-DIV linker comprises 92 amino acids, but there are only 15 residues between the end of DIIIS6 and the IFM motif. To properly occlude the intracellular mouth of the channel, 10–20 residues between the end of DIIIS6 and the IFM motif are supposed to be optimal to form the hinged-lids structures [West et al., 1992]. The mutant sodium channel expressed in our patient's muscle has an insertion of 35 amino acids preceding the IFM motif, and showed disruption of fast inactivation. Considering the number of residues between the end of DIIIS6 and the IFM motif, the 35-amino acid insertion is probably too large and may give the "lid" more freedom of movement. Indeed, it has been reported that even a 12-amino-acid insertion into the 5′ end of the DIII-DIV linker (nine residues) and the beginning part of DIVS1 (three residues) causes disruption of fast inactivation [Patton and Goldin, 1991]. Therefore, it is highly possible that the elongated loop in our mutant channel does not properly function as the hinged lid, resulting in the disruption of fast inactivation.

The abnormally spliced channel expressed in cell culture showed disruption of fast inactivation, which is consistent with the hyperexcitability of the patient's skeletal muscle. In the case of heterozygous mutations located in coding regions (missense mutations), the proportion of the mutant channel might be expected to be half of the total channel, assuming equal expression. In the heterozygous patient described here, however, the expression of the aberrantly spliced mutant channel is likely less than half of the total channel. The proportion of mRNA coding for the abnormal channel was roughly estimated from the fluorometric measurement of the PCR fragments (Fig. 2B). The abundance of the mRNA for the mutant channel isoform was about 60% that of the normal isoform (Fig. 2B). The other mRNA isoforms were out of frame and introduced premature termination codons, so they are likely to be partially degraded by nonsense-mediated mRNA decay [Chang et al., 2007]. However, it is not certain whether the mutant channel is translated, correctly folded, and targeted to the plasma membrane as efficiently as the wild type. Indeed, the current density of mutant channel was about half that of wild type when expressed in HEK-293T cells, although this might also reflect a difference in the open probability between wild-type and mutant channels. Simply by multiplying the two numbers above, the expression ratio between the wild-type and mutant channels was estimated at 10:3. Computer simulation varying the expression level of the mutant showed that repetitive firing of action potentials (myotonia) is observed even if the expression of the mutant channel is set at 15% (Fig. 5). Taken together, the most likely explanation for our observations is that the functional defect of the mutant channel caused by aberrant splicing is sufficient to cause the patient's myotonic symptoms.

In summary, we have identified a rare nondystrophic myotonia caused by a mutation in the AT-AC type II intron in *SCN4A*. Our experiments also contribute to a better understanding of the splicing mechanisms for a very rare class of introns. Henceforth, the inherited channelopathies caused by mutations in noncoding regions should be investigated more vigorously.

Acknowledgments

The authors thank Dr. Steve Cannon for providing the expression vectors, Dr. Ryuzo Mizuno for referring the patient, and Ms. Mieko Tanaka for technical assistance.

References

Armstrong CM, Bezanilla F. 1977. Inactivation of the sodium channel. II. Gating current experiments. J Gen Physiol 70:567–590.

Brow DA. 2002. Allosteric cascade of spliceosome activation. Annu Rev Genet 36: 333–360.

Burge CB, Padgett RA, Sharp PA. 1998. Evolutionary fates and origins of U12-type introns. Mol Cell 2:773–785.

Cannon SC. 2006. Pathomechanisms in channelopathies of skeletal muscle and brain. Annu Rev Neurosci 29:387–415.

Cannon SC, Brown Jr RH, Corey DP. 1993. Theoretical reconstruction of myotonia and paralysis caused by incomplete inactivation of sodium channels. Biophys J 65:270–288.

Carmel I, Tal S, Vig I, Ast G. 2004. Comparative analysis detects dependencies among the 5′ splice-site positions. RNA 10:828–840.

Chang YF, Imam JS, Wilkinson MF. 2007. The nonsense-mediated decay RNA surveillance pathway. Annu Rev Biochem 76:51–74.

Cohen JB, Snow JE, Spencer SD, Levinson AD. 1994. Suppression of mammalian 5′ splice-site defects by U1 small nuclear RNAs from a distance. Proc Natl Acad Sci USA 91:10470–10474.

Colding-Jorgensen E. 2005. Phenotypic variability in myotonia congenita. Muscle Nerve 32:19–34.

Dietrich RC, Incorvaia R, Padgett RA. 1997. Terminal intron dinucleotide sequences do not distinguish between U2- and U12-dependent introns. Mol Cell 1:151–160.

Dutzler R, Campbell EB, Cadene M, Chait BT, MacKinnon R. 2002. X-ray structure of a ClC chloride channel at 3.0 A reveals the molecular basis of anion selectivity. Nature 415:287–294.

Fournier E, Arzel M, Sternberg D, Vicart S, Laforet P, Eymard B, Willer JC, Tabti N, Fontaine B. 2004. Electromyography guides toward subgroups of mutations in muscle channelopathies. Ann Neurol 56:650–661.

Fournier E, Viala K, Gervais H, Sternberg D, Arzel-Hezode M, Laforet P, Eymard B, Tabti N, Willer JC, Vial C, Fontaine B. 2006. Cold extends electromyography distinction between ion channel mutations causing myotonia. Ann Neurol 60:356–365.

George Jr AL. 2005. Inherited disorders of voltage-gated sodium channels. J Clin Invest 115:1990–1999.

Green DS, George Jr AL, Cannon SC. 1998. Human sodium channel gating defects caused by missense mutations in S6 segments associated with myotonia: S804F and V1293I. J Physiol 510(Pt 3):685–694.

Hastings ML, Resta N, Traum D, Stella A, Guanti G, Krainer AR. 2005. An LKB1 AT-AC intron mutation causes Peutz-Jeghers syndrome via splicing at noncanonical cryptic splice sites. Nat Struct Mol Biol 12:54–59.

Hayward LJ, Brown Jr RH, Cannon SC. 1996. Inactivation defects caused by myotonia-associated mutations in the sodium channel III-IV linker. J Gen Physiol 107:559–576.

Incorvaia R, Padgett RA. 1998. Base pairing with U6atac snRNA is required for 5′ splice site activation of U12-dependent introns in vivo. RNA 4:709–718.
Kandels-Lewis S, Seraphin B. 1993. Involvement of U6 snRNA in 5′ splice site selection. Science 262:2035–2039.
Kolossova I, Padgett R.A 1997. U11 snRNA interacts in vivo with the 5′ splice site of U12-dependent (AU-AC) pre-mRNA introns. RNA 3:227–233.
Kubota T, Kinoshita M, Sasaki R, Aoike F, Takahashi MP, Sakoda S, Hirose K. 2009. New mutation of the Na channel in the severe form of potassium-aggravated myotonia. Muscle Nerve 39:666–673.
Kumakura A, Ito M, Hata D, Oh N, Kurahashi H, Wang JW, Hirose S. 2009. Novel de novo splice-site mutation of SCN1A in a patient with partial epilepsy with febrile seizures plus. Brain Dev 31:179–182.
Lehmann-Horn F, Iaizzo PA, Franke C, Hatt H, Spaans F. 1990. Schwartz-Jampel syndrome: II. Na+ channel defect causes myotonia. Muscle Nerve 13:528–535.
Lesser CF, Guthrie C. 1993. Mutations in U6 snRNA that alter splice site specificity: implications for the active site. Science 262:1982–1988.
Matthews E, Fialho D, Tan SV, Venance SL, Cannon SC, Sternberg D, Fontaine B, Amato AA, Barohn RJ, Griggs RC, Hanna MG. 2010. The non-dystrophic myotonias: molecular pathogenesis, diagnosis and treatment. Brain 133:9–22.
Mount SM, Anderson P. 2000. Expanding the definition of informational suppression. Trends Genet 16:157.
Nagamitsu S, Matsuura T, Khajavi M, Armstrong R, Gooch C, Harati Y, Ashizawa T. 2000. A "dystrophic" variant of autosomal recessive myotonia congenita caused by novel mutations in the CLCN1 gene. Neurology 55:1697–1703.
Parker R, Siliciano PG. 1993. Evidence for an essential non-Watson-Crick interaction between the first and last nucleotides of a nuclear pre-mRNA intron. Nature 361:660–662.
Patel AA, Steitz JA. 2003. Splicing double: insights from the second spliceosome. Nat Rev Mol Cell Biol 4:960–970.
Patton DE, Goldin AL. 1991. A voltage-dependent gating transition induces use-dependent block by tetrodotoxin of rat IIA sodium channels expressed in *Xenopus* oocytes. Neuron 7:637–647.
Plassart E, Eymard B, Maurs L, Hauw JJ, Lyon-Caen O, Fardeau M, Fontaine B. 1996. Paramyotonia congenita: genotype to phenotype correlations in two families and report of a new mutation in the sodium channel gene. J Neurol Sci 142: 126–133.
Roca X, Krainer AR. 2009. Recognition of atypical 5′ splice sites by shifted base-pairing to U1 snRNA. Nat Struct Mol Biol 16:176–182.
Ruan Y, Liu N, Priori SG. 2009. Sodium channel mutations and arrhythmias. Nat Rev Cardiol 6:337–348.
Schoser BG, Schroder JM, Grimm T, Sternberg D, Kress W. 2007. A large German kindred with cold-aggravated myotonia and a heterozygous A1481D mutation in the SCN4A gene. Muscle Nerve 35:599–606.
Seraphin B, Kretzner L, Rosbash M. 1988. A U1 snRNA:pre-mRNA base pairing interaction is required early in yeast spliceosome assembly but does not uniquely define the 5′ cleavage site. EMBO J 7:2533–2538.
Sheth N, Roca X, Hastings ML, Roeder T, Krainer AR, Sachidanandam R. 2006. Comprehensive splice-site analysis using comparative genomics. Nucleic Acids Res 34:3955–3967.
Siliciano PG, Guthrie C. 1988. 5′ Splice site selection in yeast: genetic alterations in base-pairing with U1 reveal additional requirements. Genes Dev 2:1258–1267.
Takahashi MP, Cannon SC. 1999. Enhanced slow inactivation by V445M: a sodium channel mutation associated with myotonia. Biophys J 76:861–868.
Tsujino A, Maertens C, Ohno K, Shen XM, Fukuda T, Harper CM, Cannon SC, Engel AG. 2003. Myasthenic syndrome caused by mutation of the SCN4A sodium channel. Proc Natl Acad Sci USA 100:7377–7382.
Wassarman DA, Steitz JA. 1992. Interactions of small nuclear RNA's with precursor messenger RNA during in vitro splicing. Science 257:1918–1925.
West JW, Patton DE, Scheuer T, Wang Y, Goldin AL, Catterall WA. 1992. A cluster of hydrophobic amino acid residues required for fast Na(+)-channel inactivation. Proc Natl Acad Sci USA 89:10910–10914.
Wu Q, Krainer AR. 1996. U1-mediated exon definition interactions between AT-AC and GT-AG introns. Science 274:1005–1008.
Wu Q, Krainer AR. 1997. Splicing of a divergent subclass of AT-AC introns requires the major spliceosomal snRNAs. RNA 3:586–601.
Wu Q, Krainer AR. 1999. AT-AC pre-mRNA splicing mechanisms and conservation of minor introns in voltage-gated ion channel genes. Mol Cell Biol 19: 3225–3236.
Zhuang Y, Weiner AM. 1986. A compensatory base change in U1 snRNA suppresses a 5′ splice site mutation. Cell 46:827–835.
Zimmer T, Surber R. 2008. SCN5A channelopathies—an update on mutations and mechanisms. Prog Biophys Mol Biol 98:120–136.

BRAIN RESEARCH 1410 (2011) 12–23

available at www.sciencedirect.com

ScienceDirect

www.elsevier.com/locate/brainres

BRAIN RESEARCH

Research Report

Astrocytic neuroprotection through induction of cytoprotective molecules; a proteomic analysis of mutant P301S tau-transgenic mouse

Kenichiro Yata[a,*], *Shinji Oikawa*[b], *Ryogen Sasaki*[a], *Akihiro Shindo*[a], *Rong Yang*[c], *Mariko Murata*[b], *Kenji Kanamaru*[d], *Hidekazu Tomimoto*[a]

[a]*Department of Neurology, Mie University Graduate School of Medicine, Tsu 514-8507, Japan*
[b]*Department of Environmental and Molecular Medicine, Mie University Graduate School of Medicine, Tsu 514-8507, Japan*
[c]*Department of Physiology, Nanjing Medical University, Nanjing 210029, China*
[d]*Departmento of Neurosurgery, Suzuka Kaisei Hospital, Suzuka 513-0836, Japan*

ARTICLE INFO

Article history:
Accepted 29 June 2011
Available online 7 July 2011

Keywords:
Tauopathy
Astrocyte
Heat shock protein 27
Peroxiredoxin 6
Apolipoprotein E
Latexin

ABSTRACT

Hyperphosphorylated tau protein constitutes a significant portion of intracellular inclusions in some neurodegenerative diseases. In addition, mutations in tau protein cause familial forms of frontotemporal dementia (FTD), indicating that dysfunction of tau protein is responsible for neurodegeneration and dementia. P301S tau-transgenic (Tg) mouse expressing human mutant tau in neurons exhibits similar features of human tauopathies including neuronal degeneration and filament accumulation consisted of hyperphosphorylated tau protein. In the present study, we attempted to characterize protein expression profiles in P301S tau-Tg mouse by using two-dimensional differential in-gel electrophoresis (2D-DIGE) coupled by peptide mass fingerprinting (PMF). As a result, we identified four upregulated proteins; heat shock protein 27 (Hsp27), peroxiredoxin 6 (Prdx6), apolipoprotein E (ApoE), and latexin (LTXN), all of which may function as a neuroprotective mechanism against tau toxicity. In immunohistochemistry, these four proteins were increased invariably in astrocytes, and these astrocytes infiltrated the area in which there are numerous accumulations of hyperphosphorylated tau and neuronal loss. Therefore, these results may indicate that astrocytes provide a neuroprotective mechanism against tau toxicity.

1. Introduction

Tau is one of the microtubule-associated proteins which play an important role in regulating microtubule assembly and stabilization, as well as maintenance of axonal transport. Under pathological conditions, tau becomes hyperphosphorylated, and is dissociated from microtubules and subsequently assembled into abnormal filaments. Tauopathy, a neurodegenerative

* *Corresponding author at:* Department of Neurology, Mie University Graduate School of Medicine, Edobashi 2-174, Tsu, 514-8507, Japan. Fax: +81 59 231 5212.
E-mail address: ken-yata@mbk.nifty.com (K. Yata).

Abbreviations: FTDP-17, frontotemporal dementia with parkinsonism linked to chromosome 17; 2D-DIGE, two-dimensional differential in-gel electrophoresis; PMF, peptide mass fingerprinting; Hsp27, Heat shock protein 27; Prdx6, Peroxiredoxin 6; ApoE, Apolipoprotein E; LTXN, Latexin; GFAP, glial fibrillary acidic protein; AD, Alzheimer's disease

0006-8993/$ – see front matter © 2011 Elsevier B.V. All rights reserved.
doi:10.1016/j.brainres.2011.06.064

disorder characterized by tau inclusions, refers to a group of increasingly recognized, adult-onset, progressive neurodegenerative diseases, including Pick's disease, progressive supranuclear palsy, corticobasal degeneration and frontotemporal dementia with parkinsonism linked to chromosome 17 (FTDP-17) (Kosik and Shimura, 2005; Lee et al., 2001). Discovery of over 30 tau gene mutations responsible for FTDP-17 clearly indicates that tau abnormalities are pivotal in neurodegeneration (Iqbal et al., 2009; Tsuboi, 2006); however, the molecular mechanisms leading to neuronal dysfunction and death remained unclear.

Tau-transgenic (Tg) mouse provides an experimental tool for defining relationships between tau mutation and neurodegeneration (Trojanowski et al., 2002). Such a model is also invaluable for developing new diagnostics and therapeutic strategy for tauopathies in humans. P301S tau-Tg mouse expressing human mutant tau in neurons exhibits an essential feature of tauopathies, including neurodegeneration and filamentous accumulation consisted of hyperphosphorylated tau protein (Allen et al., 2002; Baba et al., 2007; Bellucci et al., 2004; Delobel et al., 2008; Yoshiyama et al., 2007). This mouse exhibits numerous tau-positive neurons in the brainstem and spinal cord, and less numerously in the other brain regions including the cerebral cortex and hippocampus (Allen et al., 2002). In addition, the mouse exhibits neurological phenotypes dominated by severe paraparesis, possibly due to loss of the anterior horn cells in the spinal cord. Therefore, in the present study, we sought to identify possible alteration of protein levels related to tau mutation in the spinal cord by using two-dimensional differential in-gel electrophoresis (2D-DIGE) followed by peptide mass fingerprinting (PMF), and cellular source of these proteins by immunohistochemistry.

2. Results

2.1. *Proteomic analysis reveals differentially-expressed proteins in P301S tau transgenic mouse by 2D-DIGE*

Individual spin protein extracts from P301S tau-Tg (n=4) and wild (Wt) (n=4) mice were compared using the 2D-DIGE technique. Fig. 1A shows a representative 2D-DIGE image with spot numbers. The number of protein spots was estimated to be 1586. 2D-DIGE analyses were processed using DeCyder Differential Analysis Software (GE healthcare), which was designed specifically for 2D-DIGE experiments. 2D-DIGE analyses rendered 32 spots that exhibited statistically significant changes in their expression level between P301S tau-Tg and Wt mice (Student's t-test, $p<0.05$).

2.2. *Identification of differentially expressed proteins*

As shown in Table 1, the 32 differentially expressed spots were identified successfully as 25 proteins by PMF. We focused on any protein that showed more than a 1.5-fold difference in protein level between P301S tau-Tg and Wt samples. As a result, glial fibrillary acidic proteins (GFAPs) and four intriguing proteins were detected (spot number 1197: apolipoprotein E (ApoE), spot number 1274: latexin (LTXN), spot number 1339: heat shock protein 27 (Hsp27), and spot number 1342: peroxiredoxin-6 (Prdx6)). Figs. 1B–E shows these four selective spots showing more than a 1.5-fold difference protein level between P301S tau-Tg and Wt mice.

2.3. *Upregulation of the four proteins in P301S tau-Tg mouse by western blotting*

Spin protein samples from P301S tau-Tg (n=5) and Wt (n=5) mice were analyzed by western blotting to estimate their content of four proteins (Hsp27, Prdx6, ApoE, LTXN). The intensity of the β-actin signal was similar between two groups and was, therefore, used as an internal reference for cross-sample normalization. Fig. 2A shows a representative western blot of the four proteins. The intensity of the bands of four proteins was stronger in samples from P301S tau-Tg mice than in those from Wt mice. Upon quantification, the signal intensities of Hsp27, Prdx6, ApoE, and LTXN, were 2.8-fold, 2.1-fold, 1.4-fold, and 1.5-fold higher, respectively, in P301S tau-Tg mice than in Wt mice.

2.4. *Astrocyte activation and neuronal loss in the anterior horn of the spinal cord in P301S tau-Tg mouse*

GFAP was detected as a significantly-upregulated protein in P301S tau-Tg mouse after proteomics analysis. Thus, we performed immunostaining of GFAP in the spinal cord of P301S tau-Tg and Wt mouse (Figs. 3A–D). In Wt mouse, GFAP-positive astrocytes were distributed numerously in the white matter, and much less in the gray matter (Fig. 3A: low magnification, C: high magnification in the anterior horn). On the contrary, in P301S tau-Tg mouse (Fig. 3B: low magnification, D: high magnification in the anterior horn), these astrocytes were present in the both gray and white matters, but prominently in the anterior horn (arrow in Fig. 3B). Figs. 3E and F shows hematoxylin and eosin (HE) staining of the anterior horn of Wt and P301S tau-Tg mouse, respectively. Swollen or atrophic motor neurons were observed in P301S tau-Tg mouse.

To identify the relationship between tau accumulation and astrocyte infiltration, we compared the localization of AT8 and GFAP positive structures. In P301S tau-Tg mouse (Fig. 3G), most AT8 staining was localized to the anterior horn of the spinal cord. In a higher magnification, phosphorylated tau was accumulated in the neuronal perikarya and thread-like or punctuate structures in the neuropil (Fig. 3H). These tau-positive structures were also stained by Gallyas sliver stain (Fig. 3I). Double immunofluorescence histochemistry for GFAP (Fig. 3J), AT8 (Fig. 3K) further revealed absence of their colocalization (Fig. 3L). With immunohistochemistry for NeuN, neurons were obviously decreased in number in the anterior horn of the spinal cord (Fig. 3N: low magnification, 3P: high magnification of the anterior horn) in P301S tau-Tg mouse, compared to WT mouse (Fig. 3M: low magnification, 3O: high magnification of the anterior horn). Collectively, these data may indicate that tau accumulation led to astrocytic activation and neuronal loss.

2.5. *Upregulation of neuroprotective proteins in activated astrocytes*

To identify localization of the four upregulated proteins, we performed double immunostaining in the spinal cord of Wt and P301S tau-Tg mouse. Figs. 4A–D shows double

immunofluorescence histochemistry for Hsp27 and GFAP in the anterior horn. In P301S tau-Tg mouse (Figs. 4A–C), immunoreactivity for Hsp27 was colocalized with GFAP-immunoreactive astrocytes, but not in the neurons (arrow in Fig. 4C indicates absence of neuronal staining). On the contrary, in Wt mouse (Fig. 4D), immunoreactivity for Hsp27 was observed in the neurons of the anterior horn, but not in GFAP-immunoreactive astrocytes. Figs. 4E–H shows double immunofluorescence histochemistry for Hsp27 and GFAP in the white matter adjacent to the anterior horn. In P301S tau-Tg mouse (Figs. 4E–G), Hsp27 was obviously colocalized with GFAP in the astrocytic perikarya and their processes. Conversely, in Wt mouse (Fig. 4H), Hsp27 was expressed in the neuronal perikarya, but no staining was identified in their processes.